Beam-Based Commissioning of a Novel X-Band Transverse Deflection Structure with Variable Polarization

P. González Caminal,* F. Christie, R. D'Arcy, S. M. Jaster-Merz, R. Assmann, F. Burkart, B. Conrad, H. Dinter, M. Foese, J. Herrmann, M. Hoffmann, M. Hüning, R. Jonas, O. Krebs, S. Lederer, B. Marchetti,† D. Marx,‡ J. Mueller, J. Osterhoff, I. Peperkorn, M. Reukauff, H. Schlarb, S. Schreiber, G. Tews, T. Vinatier, M. Vogt, A. de Z. Wagner, and S. Wesch
Deutsches Elektronen-Synchrotron DESY, Notkestr. 85, 22607 Hamburg, Germany

P. Craievich, M. Bopp, H.-H. Braun, A. Citterio, R. Fortunati, R. Ganter, T. Kleeb, F. Marcellini, M. Pedrozzi, E. Prat, S. Reiche, K. Rolli, and R. Sieber
Paul Scherrer Institut, 5232 Villigen, Switzerland

A. Grudiev, W. L. Millar, N. Catalan-Lasheras, G. McMonagle, S. Pitman, V. del Pozo Romano, K. T. Szypula, and W. Wuensch
CERN, 1211 Geneva 23, Switzerland

Longitudinal electron-beam diagnostics play a critical role in the operation and control of X-ray free-electron lasers (XFELs), which rely on parameters such as the current profile, the longitudinal phase space, or the slice emittance of the particle distribution. On the one hand, the femtosecond-scale electron bunches produced at these facilities impose stringent requirements on the resolution achievable with the diagnostics. On the other, research and development of novel accelerator technologies as beam-driven plasma-wakefield accelerators (PWFA) demand unprecedented capabilities to resolve the centroid offsets in the full transverse plane along the longitudinal bunch coordinate. We present the beam-based commissioning of an advanced X-band transverse-deflection RF structure (TDS) system with the new feature of providing variable polarization of the deflecting force: the PolariX-TDS. By means of a comprehensive campaign of measurements conducted with the prototype, key parameters of the RF performance of the system are validated and a phase-space characterisation of an electron bunch is accomplished with a time resolution of 3.3 fs. Furthermore, an analysis of second-order effects induced on the bunch from its passage through the PolariX-TDS is presented.

I. INTRODUCTION

During the past two decades, X-ray free-electron lasers (XFELs) [1–6] driven by a linear accelerator (linac) have emerged as a revolutionary tool for the study of matter. By generating high-power X-ray pulses with durations ranging from several hundred femtoseconds down to a few femtoseconds, XFELs enable ultrafast time-resolved X-ray studies of molecular systems and condensed matter with atomic spatial resolution [7–9]. Both the Self-Amplified Spontaneous Emission (SASE) [10–12] and the seeding process [13–15] on which XFELs typically rely depend crucially on the current profile, the longitudinal phase space, and the slice emittance of the electron bunch. Short and intense X-ray pulses typically require a strong longitudinal electron-bunch compression, which can and normally do trigger collective effects such as coherent synchrotron radiation (CSR) or longitudinal space charge (LSC) that degrade the quality of the beam [16–18]. In order to optimise the performance of these powerful machines, the parameters of the electron bunches need to be diagnosed and controlled with temporal resolutions on the femtosecond and even sub-femtosecond scale. In a similar way, stringent requirements apply to novel high-gradient accelerator technologies such as beam-driven plasma-wakefield accelerators (PWFA) [19, 20]. In a PWFA, the large focusing fields produced within the micrometer-level accelerating structure inside the plasma place strong constraints on the extent of transverse centroid offsets along the bunch in both transverse planes [21–23]. This demands unprecedented diagnostic capabilities to resolve the longitudinal structure of the particle distribution in the full transverse plane. In this paper we present the beam-based commissioning of a novel transverse-deflection RF structure (TDS) that fulfils these requirements.

Transverse-deflection structures were developed in the 1960s as particle separators for particle-physics research [24] and gained popularity as longitudinal diagnostic devices at FELs around the 2000s [25–31]. Shortly thereafter, the need to characterise ultra-short bunches produced in low-charge FEL operation [32] triggered the development of a new generation of structures working at the X-band frequency range ($f_{RF} \approx 12$ GHz), leading to a compact hardware design and an improvement of the time resolution down to the few- and sub-femtosecond level [33–37]. Recent experiments, however, show that sub-femtosecond resolutions can also be achieved at the C-band range ($f_{RF} \approx 6$ GHz) [38]. Analogous to a streak camera, a conventional TDS system generates a linear correlation between the longitudinal coordinate ξ and either the horizontal x or the vertical y coordinate, thus enabling the

* pau.gonzalez@desy.de
† Present address: European XFEL, Holzkoppel 4, 22869 Schenefeld, Germany
‡ Present address: Brookhaven National Laboratory, Upton, NY 11973-5000, USA

measurement of the current profile and the local beam size along the bunch with a screen in the transverse plane. The supplementary use of a dipole spectrometer dispersing in the plane perpendicular to the streak enables the measurement of the longitudinal phase space. In order to avoid a rotation of the RF-fields due to mechanical imperfections of the structure, however, the standard geometry of a TDS is designed to lock the direction of the streak in a single transverse axis.

In 2016, in the framework of a study for a future compact linear collider (CLIC) [39], new compact high-power RF components operating at the X-band were devised at CERN [40], which led to a novel TDS design granting full control over the transverse direction of the streaking field. In parallel, the so-called high-precision tuning-free assembly procedure [41, 42] was developed at the Paul-Scherrer-Institut (PSI, Switzerland) to produce the C-band accelerating structures for SwissFEL [6]. The high-precision machining thereby enabled is mandatory for the production of the new structure, which requires an excellent azimuthal symmetry to avoid the deterioration of the polarization of the streaking field. At the same time, an increasing demand for new longitudinal beam diagnostics came from several research facilities: FLASHForward [43, 44], FLASH2 [45], and SINBAD-ARES [46] at DESY, and the ATHOS beamline [47] at SwissFEL at the PSI. In this context, a collaboration between DESY, PSI, and CERN was established to develop and build an advanced X-band TDS system with the new feature of providing variable polarisation of the deflecting field, namely the polarizable X-band TDS (PolariX-TDS) [48–50]. The unique capabilities of the novel device open up new perspectives for the characterisation of electron bunches, including the reconstruction of the 3D charge-density distribution in real space [51–53] or the time-resolved 4D transverse phase space [54, 55].

The first PolariX-TDS was installed in the FLASHForward facility, a test bed for precision plasma-wakefield acceleration research integrated in the Free-Electron Laser in Hamburg (FLASH) [1, 56] at DESY. In order to validate the design parameters of the prototype and assess its performance in real experimental conditions, a comprehensive commissioning campaign of beam-based measurements was conducted. The results complement two previous publications describing the RF-design [52] and the earliest experience made with electron bunches [53], thus concluding the major milestones of the collaboration after the production of the novel device.

The contents of the paper are organised as follows: Section II reviews the principles of operation of a TDS and the effects that it induces on the electron bunch; Section III gives an overview of the FLASH and FLASHForward facilities, and describes the dedicated beamline in which the PolariX-TDS is installed; details about the operation of some of its distinctive RF-components are provided in Section IV together with the specifications of the full hardware system and a short description of its commissioning; the beam-based experimental campaign is presented in Section V, including the validation of the RF performance of the device and an example application as a diagnostic of an electron bunch with special emphasis on the evaluation of TDS effects induced on the particle distribution; Section VI draws conclusions from the work presented in the paper.

II. REVIEW OF OPERATION PRINCIPLES OF A TDS

A. Bunch duration and longitudinal resolution

The electric and magnetic fields in a TDS are excited in a hybrid HEM mode with both transverse electric and magnetic fields [24, 57, 58]. In the particular case of vertical deflection, the Lorentz force experienced by a relativistic particle with charge e travelling through the device in synchronicity with the fields is given by the equations [24, 26]:

$$F_x = 0 \tag{1a}$$

$$F_y = eE_0 \sin\left(\phi_{RF} + k_{RF}\xi\right) \tag{1b}$$

$$F_z = eE_0 k_{RF} y \cos\left(\phi_{RF} + k_{RF}\xi\right), \tag{1c}$$

where $k_{RF} = 2\pi/\lambda_{RF}$ is the wavenumber of the RF field and ϕ_{RF} its phase at the location of the beam with respect to the zero crossing. For $k_{RF}|\xi| \ll 1$, the kick accrued by a particle after its propagation over the length of the device L can be approximated to first order to:

$$y'_{s=L} \approx y'_0 + \frac{eV_0}{p_0 c}\left(k_{RF}\xi\cos\phi_{RF} + \sin\phi_{RF}\right), \tag{2}$$

where $V_0 = E_0 L$ is referred to as the *integrated voltage*. From Eq. (2) it is clear that for a bunch of particles a centroid deflection occurs for $\sin\phi_{RF} \neq 0$ and a "shearing" effect is produced along the bunch, which is linear in ξ. When operating at either the first or the second zero crossing of the RF field, no net deflection takes place and the effect of the pitch is characterised by the constant K_y:

$$K_y = \pm\frac{eV_0 k_{RF}}{p_0 c}, \quad \text{for} \quad \phi_{RF} = 0, \pi. \tag{3}$$

The integrated voltage V_0 is related to the power fed into the system P_{in} by the *transverse shunt impedance* $R_\perp$:

$$V_0 = \sqrt{R_\perp P_{\text{in}}} = D\sqrt{P_{\text{in}}}, \tag{4}$$

which depends on key parameters of the RF design [59] and is very often expressed in terms of its square root, which is referred to as *power-to-voltage constant* D. The wavenumber is given by the frequency of the RF system $k_{RF} = 2\pi f_{RF}/c$. Finally, particles with a lower momentum p_0 experience a larger kick, since they are less "stiff" than particles with a larger momentum.

By choosing a suitable beam optics setup, the longitudinally varying kick $y'(\xi)$ introduced by the TDS can be used to map the longitudinal coordinate into a transverse coordinate. In this way, the measurement of the transverse beam size provides direct information about the bunch duration. Approximating the TDS by a drift plus an instantaneous kick induced in the middle of the device, the beam size measured at a screen

equals the natural beam size $\sigma_{y,\beta}$ plus the streaked beam size:

$$\sigma_{y,\mathrm{scr}}^2 = \sigma_{y,\beta}^2 + (R_{34}K_y)^2\,\sigma_\xi^2 \tag{5a}$$

$$= \sigma_{y,\beta}^2 + S_y^2\sigma_\xi^2\,, \tag{5b}$$

where the *shear parameter* $S_y = R_{34}K_y$ has been introduced. According to Eq. (5b), in order to be able to retrieve the bunch duration σ_ξ, the streaked beam size must dominate over its natural beam size $S_y\sigma_\xi > \sigma_{y,\beta}$. This leads to the definition of *longitudinal resolution* R_ξ:

$$R_\xi := \frac{\sigma_{y,\beta}}{|S_y|}, \tag{6}$$

which is the figure of merit typically used to characterise the resolution power of a TDS system. Expressing the transfer matrix element R_{34} and the natural beam size at the screen in terms of the Courant-Snyder parameters [60] and using Eq. (3), the longitudinal resolution can be expressed as:

$$R_\xi = \frac{\sqrt{\varepsilon_y}}{\sqrt{\beta_y^0}\cdot\sin\Delta\psi}\cdot\frac{p_0 c}{eV_0 k_{RF}}, \tag{7}$$

where ε_y is the geometric emittance in the streaking direction, β_y^0 is the beta function at the location of the TDS, and $\Delta\psi$ is the phase advance from the TDS to the screen. Eq. (7) shows that in order to optimise the longitudinal resolution, the phase advance should fulfil the condition $\sin\Delta\psi \approx 1$ and the beta function at the location of the TDS should be as large as possible. Notice that the resolution is independent of the beta function at the screen, which can thus be freely adjusted to fulfil further requirements of the measurement. In general, provided that the streaked beam size fits within the field-of-view (FOV) of the screen, it is desirable to set a beta function which is large enough to overcome the screen resolution [61], which adds in quadrature to the expression given in Eq. (5).

A convenient way to transport the beam from the TDS to the screen is achieved when parallel-to-point imaging conditions [62] are fulfilled:

$$\boldsymbol{R_y} = \begin{pmatrix} 0 & R_{34} \\ R_{43} & R_{44} \end{pmatrix}. \tag{8}$$

This is indeed equivalent to setting a phase advance that satisfies $\sin\Delta\psi = 1$ and $\alpha_y^0 = 0$ at the TDS entrance, where α_y is the Courant-Snyder alpha parameter of the beam in the streaking direction. As discussed in Section II C, the condition $\alpha_y^0 = 0$ is additionally required to avoid undesirable effects induced by the TDS when measuring the longitudinal phase space of the beam.

B. Current profile and slice transverse beam parameters

The current profile of the bunch is obtained from the transverse particle distribution measured at the screen by converting the streaking axis into time according to the shear parameter S_y and obtaining the projection of the image intensity to the time axis. The magnitude of the shear parameter is calculated by scanning a small range of RF phases around the zero crossing while measuring the centroid offsets at the screen $\langle y_{\mathrm{scr}}\rangle$. Approximating the $\sin\phi_{RF}$ for small RF phases in Eq. (2) and taking the first moments of the particle distribution, this can be expressed as:

$$S_y = \frac{\Delta\langle y_{\mathrm{scr}}\rangle}{\Delta\phi_{RF}}\cdot k_{RF}. \tag{9}$$

An important aspect to take into account when measuring the bunch duration and the current profile is the effect of intrinsic bunch correlations between the longitudinal coordinate and the streaking direction. The transport of the centroids at a location ξ along the bunch from the TDS entrance to the screen is given by the expression:

$$\langle y_{\mathrm{scr}}\rangle_\xi = \langle y_\beta\rangle_\xi + S_y\cdot\xi, \tag{10}$$

where $\langle y_\beta\rangle_\xi$ corresponds to the vertical centroid at the screen due to the natural betatron motion of the particles. In the absence of bunch correlations, $\langle y_\beta\rangle_\xi$ is constant along the whole bunch and the vertical screen coordinate is directly proportional to the longitudinal coordinate of the bunch $y = S_y\cdot\xi$. However, if intrinsic bunch correlations exist, the mapping between the longitudinal coordinate and the screen coordinate becomes generally a non-linear function $\mu : \xi \mapsto y$. Moreover, μ is different at each zero crossing, since S_y flips its sign whereas $\langle y_\beta\rangle_\xi$ does not, which results in two different current profiles and, consequently, two different bunch durations that are either over- or underestimated. The retrieval of the real bunch duration can be achieved by measuring the streaked beam sizes for the two zero-crossings [63]. Additionally, if μ is invertible $\mu^{-1} : y \mapsto \xi$ the bunch correlations can also be obtained and the real current profile reconstructed from the two measurements. Such a method—sometimes referred to as *two-point tomographic reconstruction*—and the conditions for its applicability are described in [64].

The measurement of the local beam size along the bunch becomes possible by analysing the beam image in the direction perpendicular to the streak. Therefore, the use of a TDS combined with conventional methods for measuring the transverse phase space [65] enables the retrieval of the slice emittance $\varepsilon_x(\xi)$, the slice Courant-Snyder parameters $\beta_x(\xi)$, $\alpha_x(\xi)$ and $\gamma_x(\xi)$, and the slice centroids $\langle x\rangle(\xi)$ and $\langle x'\rangle(\xi)$ [29, 66, 67]. Since the novel PolariX-TDS system allows the direction of the streaking field to be varied, the slice beam parameters of both the horizontal and the vertical axes can be measured with the same experimental setup [53]. Furthermore, by measuring the beam at a sufficient number of streaking angles accross the whole transverse plane and combining the images using tomographic techniques, the 3D charge density can be retrieved [52, 53, 68], which, in combination with a 2D scan of the phase advance of the beam in x and y, can be extended to the time-resolved 4D transverse phase space of the particle distribution (i.e., the full 5D phase space) [54, 55].

C. Longitudinal phase space

The longitudinal phase space becomes accessible by dispersing the beam in the direction perpendicular to the streak with a spectrometer located between the structure and the screen. In this configuration, the impact of TDS-induced effects on the measured energy distribution needs to be taken into account. According to the Panofsky-Wenzel theorem [69], the longitudinally-dependent transverse deflection imprinted by the TDS is only possible if a radially-dependent gradient of the longitudinal electric field is present in the structure: $\partial_\xi F_r = \partial_r F_z$ (cf. Eq. (1)). For bunches much shorter than the TDS length $\sigma_\xi \ll L$, the overall momentum change of the particles is dominated by the radial gradient of the longitudinal electric field and the relative momentum deviation δ at the TDS exit is [70]:

$$\delta_{s=L} \approx \delta_0 + K_y y_0 + \frac{K_y L}{2} y_0' + \frac{K_y^2 L}{6}\xi. \tag{11}$$

When considering a bunch of particles, this energy change affects the slice energy spread, the sliced relative energy deviation, and, therefore, the energy chirp of the full bunch. The resulting sliced relative energy deviation is directly obtained from Eq. (11):

$$\langle\delta_{s=L}\rangle_\xi = \langle\delta_0\rangle_\xi + K_y\langle y_0\rangle_\xi + \frac{K_y L}{2}\langle y_0'\rangle_\xi + \frac{K_y^2 L}{6}\xi. \tag{12}$$

The last term on the r.h.s. of this equation is typically referred to as the *TDS-induced energy chirp*, since it induces a linear correlation between δ and ξ. Additionally, the second and third terms indicate that in the presence of intrinsic bunch correlations between the vertical phase space and the longitudinal coordinate—i.e., $\langle y_0\rangle_\xi \neq 0$ and/or $\langle y_0'\rangle_\xi \neq 0$—the actual slice mean energy at the TDS exit might deviate from its original value. The effect of these correlations flips its sign depending on the zero crossing at which the TDS is operated, resulting in two different energy profiles. Assuming that the absolute value of the kick does not change with the zero crossing $K_y^+ = -K_y^- = |K_y|$, the true sliced relative energy deviation is obtained from the two measurements by computing the expression $K_y^+\langle\delta_-\rangle_\xi - K_y^-\langle\delta_+\rangle_\xi$, which, after rearranging terms, results in the following formula:

$$\langle\delta_0\rangle_\xi = \frac{\langle\delta_+\rangle_\xi + \langle\delta_-\rangle_\xi}{2} - \frac{|K_y|^2 L}{6}\xi, \tag{13}$$

where the subindices $+/-$ identify the measurements at each zero crossing. Notice that the comparison between the two measurements is performed in terms of ξ, which requires applying the inverted (generally non-linear) mapping from the screen coordinate to the longitudinal coordinate $\mu^{-1} : y \mapsto \xi$.

The induced slice-energy-spread growth is given by the expression:

$$\sigma_{\mathrm{IES},\xi}^2 \approx K_y^2 \varepsilon_{y,\xi}\left(\beta_{y,\xi}^0 - L\alpha_{y,\xi}^0 + \frac{L^2}{4}\gamma_{y,\xi}^0\right), \tag{14}$$

where the subindex ξ identifies a particular slice. Since the bunch is typically sent collimated with a moderately large beam size through the TDS—i.e., $\alpha_y^0 \approx 0$ and $\gamma_y^0 \approx 1/\beta_y^0 \ll 1$—the induced slice energy spread for a given slice can be approximated with:

$$\sigma_{\mathrm{IES},\xi} \approx |K_y|\sqrt{\varepsilon_{y,\xi}\beta_{y,\xi}^0}. \tag{15}$$

The product of Eq. (15) and the longitudinal resolution as given by Eq. (6) equals the geometric emittance of the beam:

$$\sigma_{\mathrm{IES},\xi} \cdot R_\xi \approx \varepsilon_{y,\xi}, \tag{16}$$

which reveals that there is a trade-off between longitudinal resolution and TDS-induced slice energy spread that imposes a fundamental limit on the achievable accuracy of the measurement [71].

Experimentally, the slice energy spread is obtained by measuring the dispersed beam size at the location of the screen. The transverse beam size in a dispersive location has two contributions: the component due to dispersion and the natural beam size, which for relativistic beams and an horizontal dispersion can be approximated by $D_x\sigma_{\delta,0}$ and $\sigma_{x,\beta} = \sqrt{\varepsilon_x\beta_x}$, respectively—where D_x is the lattice dispersion at the screen, ε_x is the geometric emittance, and β_x is the beta function at the screen. The term corresponting to the natural beam size, leads to the definition of the *energy resolution* of the measurement:

$$R_\delta := \frac{\sigma_{x,\beta}}{|D_x|} = \frac{\sqrt{\varepsilon_x\beta_x}}{|D_x|}, \tag{17}$$

which can be optimised by maximising the dispersion and minimising the beta function at the screen. Additionally, the measurement is affected by the TDS-induced slice energy spread introduced in Eq. (14) and the screen resolution R_{scr}:

$$\sigma_{x,\mathrm{scr}}^2 = R_{\mathrm{scr}}^2 + \sigma_{x,\beta}^2 + D_x^2\left(\sigma_{\delta,0}^2 + \sigma_{\mathrm{IES}}^2\right). \tag{18}$$

Notice that the subindex ξ identifying the location along the bunch has been dropped for simplicity—except for the screen resolution R_{scr}, which is independent of the beam parameters. The contribution of each of the terms in Eq. (18) can be precisely determined by means of dedicated measurements [72, 73]. Alternatively, they can be estimated from knowledge of the evolution of the beam parameters along the beamline, the dispersion at the screen, and the specifications of the screen. The latter is the approach followed in this paper (cf. Section V D).

If the second moments of the distribution are transported all the way from the TDS entrance down to the spectrometer screen, a correlation between the horizontal and vertical spatial axes emerges [74]:

$$\langle x_{\mathrm{scr}} y_{\mathrm{scr}}\rangle_\xi = D_x S_y \varepsilon_{y,\xi}\left(-\alpha_{y,\xi}^0 + \frac{L}{2}\gamma_{y,\xi}^0\right), \tag{19}$$

If either optimal transport conditions are fulfiled or the two terms inside the brackets on the r.h.s. of Eq. (19) cancel each other, the induced correlation is zero. Otherwise, the longitudinal phase space of the examined slice becomes sheared. Considering an infinitessimally thin slice and assuming that the transverse phase space of the bunch in x and y are completely decoupled from each other, two figures of merit that permit the characterisation of this effect are:

1. the Pearson coefficient of the beam matrix in the transverse plane x–y:

$$\rho_{x,y} = \frac{\langle x_{\mathrm{scr}} y_{\mathrm{scr}} \rangle_\xi}{\sqrt{\langle x_{\mathrm{scr}}^2 \rangle_\xi} \cdot \sqrt{\langle y_{\mathrm{scr}}^2 \rangle_\xi}}, \tag{20}$$

where $\langle x_{\mathrm{scr}}^2 \rangle_\xi = D_x^2(\sigma_{\delta,0}^2 + \sigma_{\mathrm{IES}}^2) + \sigma_{x,\beta}^2$ and $\langle y_{\mathrm{scr}}^2 \rangle_\xi = R_{34}^2 \varepsilon_{y,\xi} \gamma_{y,\xi}^0$,

2. the angle of the resulting tilt with respect to the energy axis, which in this case would be the horizontal:

$$\theta_{x,y} = \arctan\left(\frac{\langle x_{\mathrm{scr}} y_{\mathrm{scr}} \rangle_\xi}{\langle x_{\mathrm{scr}}^2 \rangle_\xi} \right). \tag{21}$$

Notice that in the presence of intrinsic bunch correlations ξ–y' and/or ξ–y, the centroid of each slice in the longitudinal-phase-space screen becomes shifted in x (energy) and y (time), and these shearing effects might have an impact on the measured slice energy spread depending on the zero crossing at which the TDS is operated.

III. EXPERIMENTAL FACILITY

The PolariX-TDS is installed in the FLASHForward experimental facility [44], a test bed for precision beam-driven plasma-wakefield research aiming to accelerate high-quality electron beams from the FLASH linac at high gradients $\gtrsim 1$ GeV/m in a few centimetres of ionized gas. It occupies a third beamline at the soft X-ray FEL user-facility FLASH [1, 56, 75]. The schematic layout of the linac and its three beamlines is shown in Fig. 1a. The different parts of the experimental setup are described in the following sections.

A. FLASH injector

At the FLASH injector, the electrons are extracted from a photo cathode [76] and are immediately accelerated inside a normal conducting 1.3-GHz RF cavity to an energy of 5.6 MeV [56]. Further acceleration to a maximum energy of 1.25 GeV is done by seven superconduction RF modules also operating at 1.3 GHz. A third-harmonic module [77] is located after the first acceleration stage in order to linearise the longitudinal phase space of the bunch for efficient compression, which is carried out by two magnetic chicanes operating in the horizontal plane [56, 78]. A kicker-septum system [79] enables the simultaneous operation of the FLASH1 and FLASH2 beamlines by extracting a fraction of the bunches contained in a bunch train. An additional dipole magnet located at the end of the FLASH2 extraction arc enables switching between FLASH2 and FLASHForward. This setup provides the three beamlines attached to the linac with GeV-scale electron bunches with charges up to 2 nC, durations of 50–5000 fs rms, currents up to 2.5 kA, a normalised slice emittance on the order of 1 µm, an uncorrelated energy spread below 0.1 % and a tunable longitudinal phase space [56].

B. FLASHForward beamline

The FLASHForward beamline [80] shares the experimental area with FLASH2 and is organised as follows. A 30-m-long dispersive section provides 4 m transverse separation with respect to FLASH2 and enables precise current-profile shaping for plasma-wakefield experimentation by means of a three-component energy collimator [81]. After the extraction, a 13-m-long straight section is dedicated to match the beam envelope to the lattice optic and finally focus it into the plasma, which is produced in a gas cell placed in a dedicated plasma-interaction chamber. Immediately after the chamber, a shorter 7-m-long section houses a broadband and a narrowband energy spectrometer, which is used for beam diagnostics. The PolariX-TDS beamline [82], schematically depicted in Fig. 1b, extends the diagnostic capabilities of FLASHForward, enabling the optimisation and characterisation of the time-resolved phase space of electron bunches before and after plasma interaction [74].

C. PolariX-TDS beamline

The major constraint imposed on the PolariX-TDS beamline design is dictated by the location of the RF-power source of the TDS, which must be close enough to the structure to minimise power losses produced along the waveguide network. As part of the PolariX-TDS collaboration, both FLASHForward and FLASH2 have their own structures. Since these beamlines cannot be operated in parallel, they share the same RF-power system in order to reduce financial costs. In this configuration, the input RF pulse delivered by a klystron is compressed by an X-band Barrel Open Cavity (XBOC) pulse compressor [40, 52] and is directed to either of the two beamlines by means of a variable power splitter [40]. At the time at which the experimental campaign presented here was performed, however, only the klystron and the waveguide network connecting it to the structure of FLASHForward were available, which is indicated with the solid red lines in Fig. 1a. The low-level RF (LLRF) system and the modulator for the klystron are located in a technical corridor outside the experimental area to ease the access for maintenance and avoid problems arising from radiation damage. On account of the aforementioned, and due to the limited space availability in the pre-existing FLASH2 beamline, the TDS at FLASHForward is located approximately 25 m downstream of the plasma-interaction chamber.

The magnetic lattice upstream of the structure is composed of 9 quadrupoles (the first 4 acting as 2 doublets), which provide enough flexibility to both match the beam envelope to the desired parameters at the entrance of the TDS and scan the

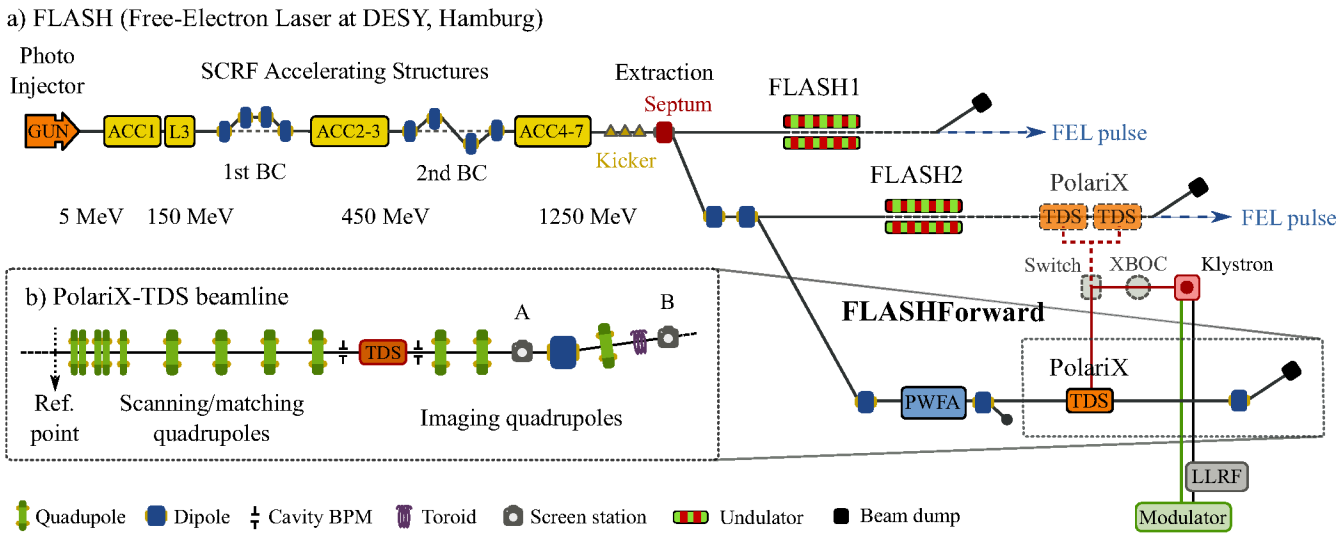

FIG. 1. a) Schematic layout of the FLASH facility with its three parallel beamlines: FLASH1, FLASH2, and FLASHForward, including the key RF components of the PolariX-TDS system (see text for details). b) Schematic layout of the PolariX-TDS diagnostics beamline. The quadrupoles upstream of the TDS are used to adjust the beam parameters at the TDS entrance and scan the phase advance in slice emittance measurements, whereas those downstream are used to adjust the transport optics for optimal longitudinal and energy resolutions. Screen station A is used to measure the sliced transverse beam parameters and the slice emittance, while screen B, located at the end of the dispersive section, is used to measure the longitudinal phase space.

phase advance when performing transverse-phase-space measurements. A 7.5-m-long section located immediately downstream of the structure is dedicated to the measurement of the longitudinally sliced transverse beam parameters and contains a screen station (A in Fig. 1b) and two quadrupoles to optimise the beam transport. After that, a 7.6-m-long dispersive section is dedicated to the diagnostic of the longitudinal phase space, which is composed of a dipole, which introduces a horizontal deflection of 5 deg, a quadrupole to add flexibility to the simultaneous optimisation of the longitudinal and energy resolutions, and a second screen station (B in Fig. 1b).

The beamline is equipped with further conventional beam diagnostics, including a toroidal current transformer located in front of the longitudinal-phase-space screen and several beam-position monitors (BPM). The BPMs around the structure are of the cavity type [83], which have a resolution of 1 µm and allow precise monitoring of the beam trajectory through the device. The screen stations [84] use an inorganic scintillator material in order to avoid coherent effects in the emission of optical transition radiation (OTR) triggered by high-brightness beams in conventional OTR monitors. The scintillator material used is Cerium-doped Gadolinium Aluminium Gallium Garnet (GAGG:Ce) and has a thickness of 200 µm. A movable screen holder, accommodating up to two different screens, and a test chart for calibration purposes is positioned to intercept the beam perpendicular to the direction of propagation. The emitted light is observed at 45 deg and is imaged out of vacuum into a CCD camera by means of an optical system exploiting the Scheimpflug principle to minimize depth-of-focus effects. The camera used is a Basler avA2300-25gm with a pixel size of 5 µm $\times$ 5µm and a total of 1760 $\times$ 2360 pixels. The nominal spatial resolution of the system is $R_{scr} \approx 10$ µm [84]. The field of view (FOV) of screen A is manually adjusted to obtain a magnification factor of 1:1, covering an area of 9 mm $\times$ 12 mm, whereas that of screen B is adjusted to a magnification factor of 2:1, resulting in an area of 18 mm $\times$ 24 mm.

IV. POLARIX-TDS HARDWARE SYSTEM

The complete PolariX-TDS hardware system used during the commissioning campaign is schematically depicted in Fig. 2 and consists of three subsystems: the PolariX-TDS itself, the RF-power source, and the low-level RF (LLRF) system. The following description of the PolariX-TDS operation is based on the more detailed account given in references 40 and 52.

An input RF pulse coming from the RF power source is split into two signals by a 3-dB E-hybrid. One of the two split arms contains a variable phase shifter to adjust the relative phase between the two signals, which are then recombined using a circular waveguide TE_{11} rotating mode launcher—referred to as an E-rotator. Depending on which E-rotator input is used to feed the power, the launched mode at the circular waveguide rotates either counterclockwise $\boldsymbol{E}_L$ or clockwise $\boldsymbol{E}_R$. If, instead, two signals with the same amplitude $E_L = E_R$ are fed simultaneously into each input—as foreseen for nominal operation—the overlap between the two rotating modes results in a linearly polarised TE_{11} mode, the polarisation of which is determined by the phase difference between the two

input signals:

$$\boldsymbol{E}_X = 2E_0 \cos(\omega_{RF} t)\hat{\boldsymbol{x}} \quad \text{for} \quad \phi_L = \phi_R, \tag{22a}$$

$$\boldsymbol{E}_Y = 2E_0 \sin(\omega_{RF} t)\hat{\boldsymbol{y}} \quad \text{for} \quad \phi_L = \phi_R + \pi\,, \tag{22b}$$

where $E_0 = E_L = E_R$, and $\hat{\boldsymbol{x}}$ and $\hat{\boldsymbol{y}}$ are the unitary vectors of the horizontal and vertical axis, respectively. By adjusting the relative phase between the two signals with the variable phase shifter, the polarisation of the TE_{11} mode can be continuously varied over the full transverse plane. This mode is launched into the structure, which supports both degenerate TM_{11}-like dipole modes due to its azymuthal symmetry. At the output, a second E-rotator operated in the opposite direction splits the RF field into its two rotating components, which are directed into two separate waveguides terminated individually with RF loads. The TDS itself is a constant-impedance circular disk-loaded waveguide structure operating in the backward-travelling-wave regime—i.e., the power (group velocity) flows in the direction opposite to the beam propagation (phase velocity), as indicated in Fig. 2. The exact resonant frequency of the structure is $f_{RF} = 11.9888$ GHz, which is adjusted by means of a precise temperature stabilisation system (not indicated in the figure) operated at $T = 65\,^{\circ}\mathrm{C}$.

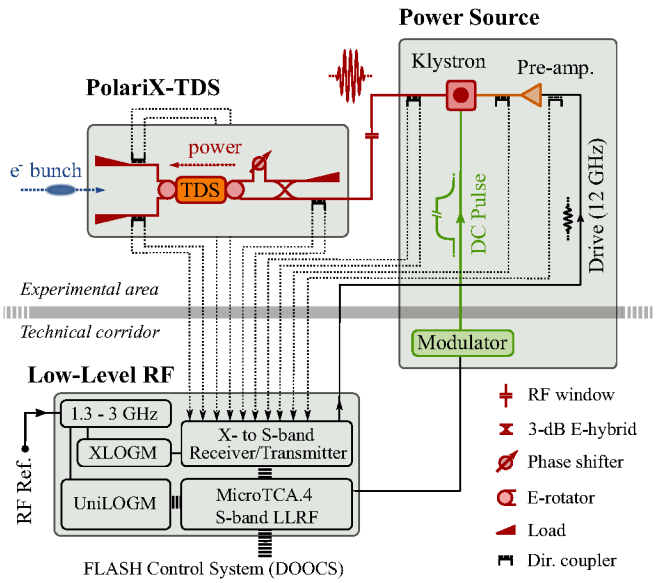

FIG. 2. Overview of the complete PolariX-TDS hardware system used during the beam-based commissioning campaign, including its three subsystems: the PolariX-TDS itself, the RF-power source, and the low-level RF (LLRF) system. For the sake of simplicity and legibility, water and vacuum systems are excluded from the figure.

The klystron (6 MW Toshiba E37113A) operates as an amplifier that converts some of the DC energy input carried by a high-voltage (≈ 160 kV), high-current (≈ 100 A) pulse delivered by a modulator (Ampegon PPT Type-μ M-Class) into RF energy with a frequency of ≈ 12 GHz given by a pre-amplified drive signal delivered by the LLRF system. The drive signal is thus amplified up to a maximum of 6 MW and is subsequently directed from the klystron output to the TDS through a waveguide network. At high power, the system is kept at ultra-high vacuum (UHV) conditions with pressures below $p < 1 \cdot 10^{-9}$ mbar. For reasons of machine safety, an RF window decouples the UHV of the klystron network from that of the structure and the components attached directly to it. Several directional waveguide couplers are used to pick up a small fraction (≈ -60 dB) of the power at different locations accross the system. At low power—before and after the pre-amplifier—only the forward signal is measured, whereas at high power the reflected signal is also provided for diagnostic and interlock purposes. Since the PolariX-TDS is the first X-band RF structure installed at DESY, a dedicated LLRF system [85] has been developed to extend the already existing systems operating at 1.3 GHz and 3 GHz to the 12 GHz required by the new device. The 12 GHz signals coming from the directional couplers are converted into the 3 GHz domain at which the MicroTCA.4 S-band LLRF module operates, enabling the integration of the hardware system into the control and data acquisition system of FLASH [86].

The structure itself was produced at PSI following the high-precision tuning-free assembly procedure [41] and was tested at the same facility before being pre-conditioned at CERN together with the remaining core RF components of the PolariX-TDS system [50, 52, 87]. The performance of all individual waveguide parts was qualified for operation at DESY. Once assembled in the FLASHForward experimental area and evacuated to UHV conditions, an automated conditioning algorithm was used to progressively increase the RF-power and the pulse length fed into the system. At the time of the beam-based commissioning campaign, the hardware was ready to be operated at full klystron power (6 MW) with RF pulses of 400 ns flat-top plus a linear decay of 100 ns. The calibration of the LLRF-components chain attached to the directional couplers was performed with an external low-power RF-signal generator and its performance at high power was subsequently benchmarked with the specifications of the klystron, achieving a level of agreement of around 10 %. The error associated with all the power measurements discussed in this paper is therefore fixed to ± 0.5 dB.

V. EXPERIMENTAL RESULTS

For the beam-based commissioning campaign, a bunch with a charge of $Q \approx 250$ pC, an energy of $\langle E \rangle = 750$ MeV, an rms duration of $\sigma_\xi \approx 280$ fs (84 μm), a FWHM projected energy spread of $\sigma_\delta \approx 0.5$ %, and a negative linear chirp was utilised. The beamline-setup routine consists of successively minimising the lattice dispersion at the end of the FLASH2 and the FLASHForward extraction sections, then matching the beam to symmetric optics at the start of the PolariX-TDS beamline ("Ref. point" in Fig. 1b) with $\beta_x = \beta_y = 10$ m and $\alpha_x = \alpha_y = 0$, which is required for the diagnostics applications discussed in Section V D. In order to reduce chromatic effects during the matching routine, the beam was energy-collimated in the dispersive section to approximately $1/3$ of its total charge, which, due to the intentional linear relation in longitudinal phase space, enables a bespoke selection of a

longitudinal region around the core of the bunch. The lattice optics downstream of the matching location is adjusted to the requirements of each measurement separately.

A. Input-power balance

As described in Section IV, the nominal operation of the PolariX-TDS requires the feeding of two RF signals with the same amplitude to each of the E-rotator inputs. If the signals are not well balanced $E_L \neq E_R$, the overlap between the two rotating modes at the circular waveguide results in an elliptically polarised mode $\boldsymbol{E}_E$. For vertical streaking this can be expressed as (cf. Eq. (22b)):

$$\boldsymbol{E}_E = E_X \cos(\omega_{RF} t)\hat{\boldsymbol{x}} + E_Y \sin(\omega_{RF} t)\hat{\boldsymbol{y}} \,, \tag{23}$$

where $E_X = E_L - E_R$ and $E_Y = E_L + E_R$. Since the two components have a phase difference of 90 deg, a bunch travelling through the PolariX-TDS at the zero crossing of the vertical field experiences not only a ξ-dependent kick in the vertical direction, but also a net deflection in the horizontal.

In order to detect the presence of such power-imbalance effects and determine their magnitude, a full 360-deg RF-phase scan is performed while observing the bunch centroid at the screen A, see Fig. 1b. To stay within the field of view (FOV) of the camera system and being sensitive to small horizonal centroid changes while streaking in the vertical plane, the power fed into the TDS must be reduced and the lattice optics must be such that the R_{12} is enhanced compared to the R_{34}. Since parallel-to-point imaging conditions are not fulfilled, both transport coffiecients R_{11} and R_{33} have to be taken into account. According to Eqs. (2) and (23), the centroid offsets measured at the screen are:

$$\langle x \rangle - \langle x_\beta \rangle = \left(R_{11}\frac{L}{2} + R_{12} \right) \frac{eV_X}{p_0 c} \cos\phi_{RF} \,, \tag{24a}$$

$$\langle y \rangle - \langle y_\beta \rangle = \left(R_{33}\frac{L}{2} + R_{34} \right) \frac{eV_Y}{p_0 c} \sin\phi_{RF} \,, \tag{24b}$$

where $\langle x_\beta \rangle$ and $\langle y_\beta \rangle$ are the centroid coordinates associated to the natural betatron motion of the beam, L is the length of the structure, and $V_X = E_X L$ and $V_Y = E_Y L$ are the integrated voltages in x and y, respectively.

The results of the measurement are shown in Fig. 3. The path described by the centroid on the screen is shown on the left plot, in which the elliptical shape resulting from the power imbalance can be clearly observed. During the measurement, the streak direction was not perfectly adjusted such that the ellipse is slightly rotated accordingly. Accounting for it, the centroid offsets are calculated by projecting the measured data onto the axes of the ellipse. The right plot shows the integrated voltage in x and y calculated from Eq. (24) versus the full range of scanned RF-phases, in which $\boldsymbol{V_X} = V_X \cos\phi_{RF}$ and $\boldsymbol{V_Y} = V_Y \sin\phi_{RF}$. Notice that the voltage in the horizontal plane has been scaled by a factor 10 to better appreciate its sinusoidal behavior.

From Eq. (23), the integrated voltage associated with the left and the right E-rotator inputs can be calculated from the vertical and horizontal terms obtained from the scan:

$$V_L = \frac{V_Y + V_X}{2} = 0.92 \text{ MV} \tag{25a}$$

$$V_R = \frac{V_Y - V_X}{2} = 0.83 \text{ MV}, \tag{25b}$$

which indicates that the left input receives 55 % of the total power fed into the system, whereas the right input only receives 45 %. The observed imbalance can be associated with a mismatch between the impedances attached to each of the two outputs of the 3-dB E-hybrid. According to RF simulations of an analogous system, a moderate mismatch factor of ~ 1.25 accounts for the $20 \cdot \log_{10}(0.83/0.92) \approx -0.9$ dB difference between the two splitter outputs, leading to a reflection-attenuation coefficient of $10 \cdot \log_{10}(P_{\text{refl}}/P_{\text{forw}}) = -19.4$ dB at its input, where P_{refl} and P_{forw} are the reflected and forward power, respectively. This is indeed consistent with the power readings obtained from the directional coupler located before the splitter, from which a reflection attenuation of -19.5 dB is obtained.

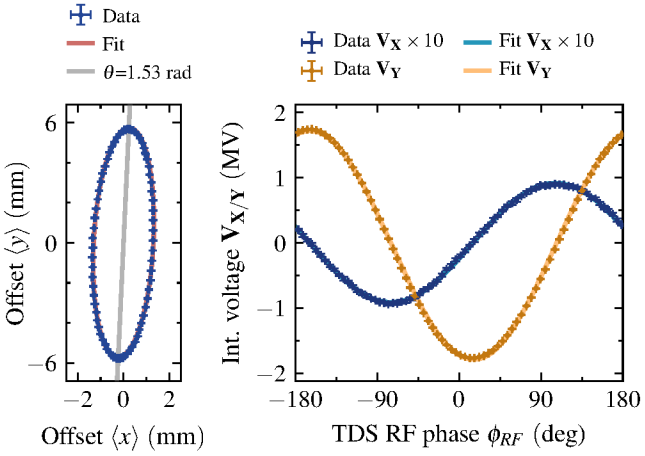

FIG. 3. 360-deg RF-phase scan performed to measure the power imbalance between the left and right inputs of the E-rotator. Left: path described by the beam centroid at the screen. RF: horizontal and vertical integrated voltages versus the RF phase (cf. Eq. (24)). Notice that the horizontal component has been scaled by a factor 10 to better appreciate its sinusoidal behavior.

A possible way to overcome this behavior would be to replace the 3-dB E-hybrid by a variable splitter, which would permit free adjustment of the power fed into each of the two E-rotator inputs to compensate for the mismatch-induced imbalance. Alternatively, as shown in Ref. 88, with hardware configurations comprising two RF structures and three phase shifters, the residual kick can also be completely eliminated. We notice, however, that the effect observed in the measurement presented in this paper does not hinder the use of the PolariX-TDS for beam diagnostics.

B. Power-to-voltage constant D

As described in Section II, the power-to-voltage constant D (cf. Eq. (4)) is an important figure of merit of the RF design representing the conversion efficiency between the power fed into the structure P_{in} and the integrated voltage V_0 experienced by the deflected particles. The power fed into the structure is calculated from the power measured at the directional coupler located before the 3-dB E-hybrid by taking into account an attenuation of 0.1 dB/m along the waveguide network (cf. Fig. 2). To obtain the integrated voltage, the shear parameter needs to be measured first (cf. Eq. (9)). The integrated voltage is then related to the shear parameter by the general expression:

$$V_0 = \frac{p_0 c}{e k_{RF}} \left(R_{33} \frac{L}{2} + R_{34} \right)^{-1} S_y. \tag{26}$$

For the measurement, V_0 is computed for five different klystron power values between 20 % and 100 % at each of the two zero crossings, and the power-to-voltage constant is subsequently calculated by means of Eq. (4). Since only the centroids are of importance, the magnetic lattice is not required to fulfil optimal-resolution constraints. On account of that, the two quadrupoles between the TDS and the screen are switched off to minimise possible errors in the transport matrix and the beam envelope in the streaking direction is sent converging through the TDS. The result is shown in Fig. 4, with an obtained value of $D = 5.1 \pm 0.1$ MV/$\sqrt{\text{MW}}$, in excellent agreement with the design parameter reported in [52]: $D = 5.2$ MV/$\sqrt{\text{MW}}$.

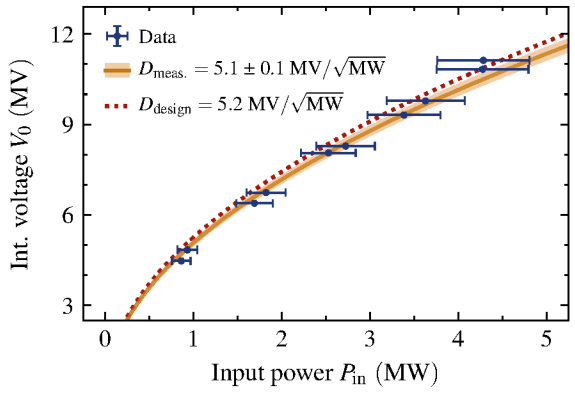

FIG. 4. Determination of the power-to-voltage constant D. Experimentally, beam-based measured integrated voltage vs. power readings. Error is dominated by power readings.

C. RF stability

The accuracy of any measurement performed with the TDS relies on the stability of the shear parameter S_y and the ability to precisely determine its magnitude. Both of these aspects are affected by fluctuations of the high-power signal that can be decomposed in two contributions:

- *RF-phase jitter* $\bar{\sigma}_\phi$, which refers to spurious variations of the phase relative to the timing reference of the accelerator,
- *RF-amplitude jitter* $\bar{\sigma}_A$, which refers to spurious variations of the amplitude that directly translate into variations of the shear parameter $\bar{\sigma}_S = |S_y| \bar{\sigma}_A$.

The experimental determination of S_y is obtained by measuring the beam centroid offsets at the screen while operating the TDS at small RF phases around the zero crossing (cf. Eq. (9)). The effect of different sources of jitter on the centroid can be evaluated by transporting the first moments of the bunch from the TDS entrance to the screen (cf. Eqs. (2) and (8)) and propagating errors. Since $\langle \xi \rangle = 0$ by definition, this leads to the following expression:

$$\bar{\sigma}^2_{\langle y \rangle} = \bar{\sigma}^2_{\langle y \rangle,\beta} + \frac{S_y^2}{k_{RF}^2} \cdot \left\{ \left[\bar{\sigma}_\phi^2 + (k_{RF} c \bar{\sigma}_t)^2 \right] \cdot \cos^2 \phi_{RF} + \bar{\sigma}_A^2 \cdot \sin^2 \phi_{RF} \right\}, \tag{27}$$

where $\bar{\sigma}_{\langle y \rangle,\beta}$ is the linac-pointing jitter measured at the screen with the TDS switched off and $\bar{\sigma}_t$ is the arrival-time jitter of the bunch. When operating around the zero crossing—i.e. $\sin \phi_{RF} \approx 0$—the last term inside the curly brackets can be neglected. Therefore, the centroid jitter at the screen $\bar{\sigma}_{\langle y \rangle}$ is dominated by the RF-phase and the arrival-time jitter, which leads to the definition of the *effective RF-phase jitter* $\bar{\sigma}_{\phi,\text{eff}}$:

$$\bar{\sigma}^2_{\phi,\text{eff}} = \bar{\sigma}_\phi^2 + (k_{RF}\, c\, \bar{\sigma}_t)^2. \tag{28}$$

In order to estimate its magnitude, the data from the power-to-voltage measurements discussed in the previous section is analysed according to the following procedure: for all the measurements of the shear parameter S_y, the mean of the centroid jitter observed at each RF-phase scan step is calculated together with the spread of the sample means, and the computed values are subsequently fitted to Eq. (27)—neglecting the RF-amplitude jitter. The linac-pointing jitter has a value of $\bar{\sigma}_{\langle y \rangle,\beta} \approx 20$ µm and is substracted in quadrature from the other terms. The result of the measurement is shown in Fig. 5, with an obtained effective RF-phase jitter of $\bar{\sigma}_{\phi,\text{eff}} = 0.097 \pm 0.003$ deg (22.4 ± 0.7 fs). A detailed analysis of the RF signal measured at the klystron output [85] indicates a phase jitter of $\bar{\sigma}_\phi = 0.033$ deg (7.7 fs). By comparing the two measurements, it derives that the main contribution to the centroid jitter at the screen is related to the arrival-time jitter of the bunch, which, according to Eq. (28), has a value of $\bar{\sigma}_t = 0.091$ deg (21.1 fs), in very good agreement with independent measurements performed at FLASH [56, 89]. This result allows to conclude that the good performance of the RF system enables a precise determination of the arrival-time jitter of the linac and that it does not compromise the accuracy of the measured shear parameter S_y.

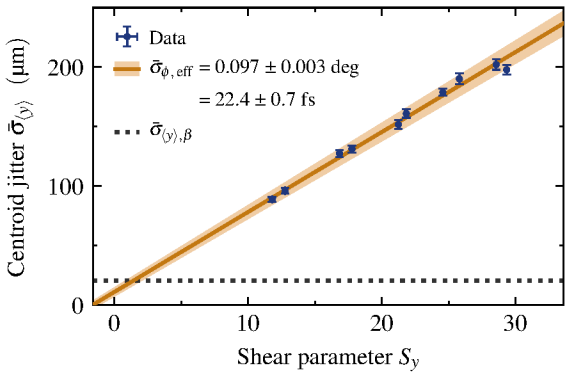

FIG. 5. Effective RF-phase jitter $\bar{\sigma}_{\phi,\mathrm{eff}}$ calculated by correlating the beam-centroid jitter measured at the screen in the streaking direction $\bar{\sigma}_{\langle y\rangle}$ with the shear parameter S_y measured at different amplitudes.

The effect of the RF-amplitude jitter $\bar{\sigma}_A$ when operating at phases around the zero crossing is mainly reflected in variations of the streaked beam size measured at the screen $\bar{\sigma}_{\langle y^2\rangle}$, which is indistinguishable from variations of the bunch duration induced in the linac $\bar{\sigma}_{\langle \xi^2\rangle}$. By propagating errors in Eq. (5b) and assuming that the unstreaked beamsize $\sigma_{y,\beta}$ remains approximately constant, the combined effect of these two jitter sources can be expressed as:

$$\bar{\sigma}^2_{\langle y^2\rangle} = S_y^2\,\sigma_\xi^2\left[\bar{\sigma}_A^2 + \left(\frac{\bar{\sigma}_{\langle \xi^2\rangle}}{\sigma_\xi}\right)^2\right]. \tag{29}$$

Notice that if the measurement is dominated by the amplitude jitter, the beamsize variations observed at the screen are approximately inversely proportional to the shear parameter, since the signal-to-noise ratio of the RF system decreases with the amplitude of the klystron power—i.e., $\bar{\sigma}_A \propto 1/\sqrt{P_{\mathrm{in}}}$.

The relative variation of the streaked beamsize at the screen is calculated for the different shear parameters obtained in the power-to-voltage measurement discussed in the previous section. The results are shown in Fig. 6, with the measured (rms) beam sizes at the top and their relative error at the bottom. The fact that the data does not show any dependence on the shear parameter implies that the amplitude jitter does not dominate the measurement and, therefore, the relative beamsize variations can be averaged together $\bar{\sigma}_{\langle y^2\rangle}/\sigma_y = 3.6 \pm 0.4$ %. An analysis of the RF signal measured at the klystron output at full power, indicates an amplitude jitter of $\bar{\sigma}_A = 0.051$ % [85]. On account of these two considerations, it is justified to deduce that the major contribution to the beam-size variations measured at the screen are caused by variations of the bunch duration induced in the linac, which, according to Eq. (29), would have a value of $\bar{\sigma}_{\langle \xi^2\rangle}/\sigma_\xi = 3.6$ %. Such variations strongly depend on the specific working point at which the linac is operated and the determination of its magnitude independently of the TDS measurements would require the use of complementary longitudinal diagnostics—e.g. a bunch compression monitor [90]—which were not available during the commissioning campaign. Nonetheless, the observed variations agree well with typical FLASH values, which supports the argument that the performance of the RF system is good enough to enable the measurement of the actual bunch duration with an accuracy better than 0.1 %.

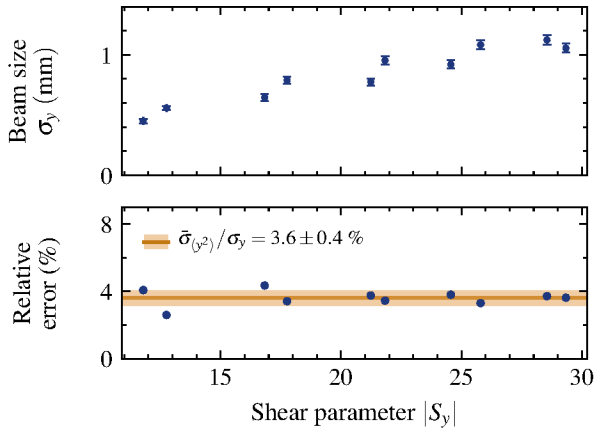

FIG. 6. Measurement of relative (streaked) beamsize variations at the screen $\bar{\sigma}_{\langle y^2\rangle}/\sigma_y$. Top: streaked beam size measured at the two zero crossings and at shear parameters S_y with an increasing magnitude. Bottom: the relative error of the measured streaked beam size provides direct information about the bunch-duration jitter induced in the linac.

D. Bunch characterisation and effective longitudinal resolution

To illustrate the diagnostic capabilities of the novel PolariX-TDS, a time-resolved phase-space reconstruction of the electron bunch used in the commissioning campaign is performed. The reconstruction is based on the independent measurement of the slice emittance in both x and y, and the longitudinal phase space, which enables the retrieval of the first moments of the six dynamic variables—i.e., $\langle x\rangle_\xi$, $\langle x'\rangle_\xi$, $\langle y\rangle_\xi$, $\langle y'\rangle_\xi$, $\langle \xi\rangle$, and $\langle \delta\rangle_\xi$—together with the following terms of the covariance matrix of the particle distribution:

$$\boldsymbol{\Sigma}_\xi = \begin{pmatrix} \langle x^2\rangle_\xi & \langle xx'\rangle_\xi & 0 & 0 & 0 & 0 \\ \langle x'x\rangle_\xi & \langle x'^2\rangle_\xi & 0 & 0 & 0 & 0 \\ 0 & 0 & \langle y^2\rangle_\xi & \langle yy'\rangle_\xi & 0 & 0 \\ 0 & 0 & \langle y'y\rangle_\xi & \langle y'^2\rangle_\xi & 0 & 0 \\ 0 & 0 & 0 & 0 & \langle \xi^2\rangle & 0 \\ 0 & 0 & 0 & 0 & 0 & \langle \delta^2\rangle_\xi \end{pmatrix}, \tag{30}$$

where the subindex ξ identifies a particular slice along the bunch with a width corresponding to the longitudinal resolution $\sqrt{\langle \xi^2\rangle} = R_\xi$.

The reference point in the slice-emittance measurements is located at the start of the PolariX-TDS beamline (cf. Fig. 1), at which the beam envelope has been previously matched to

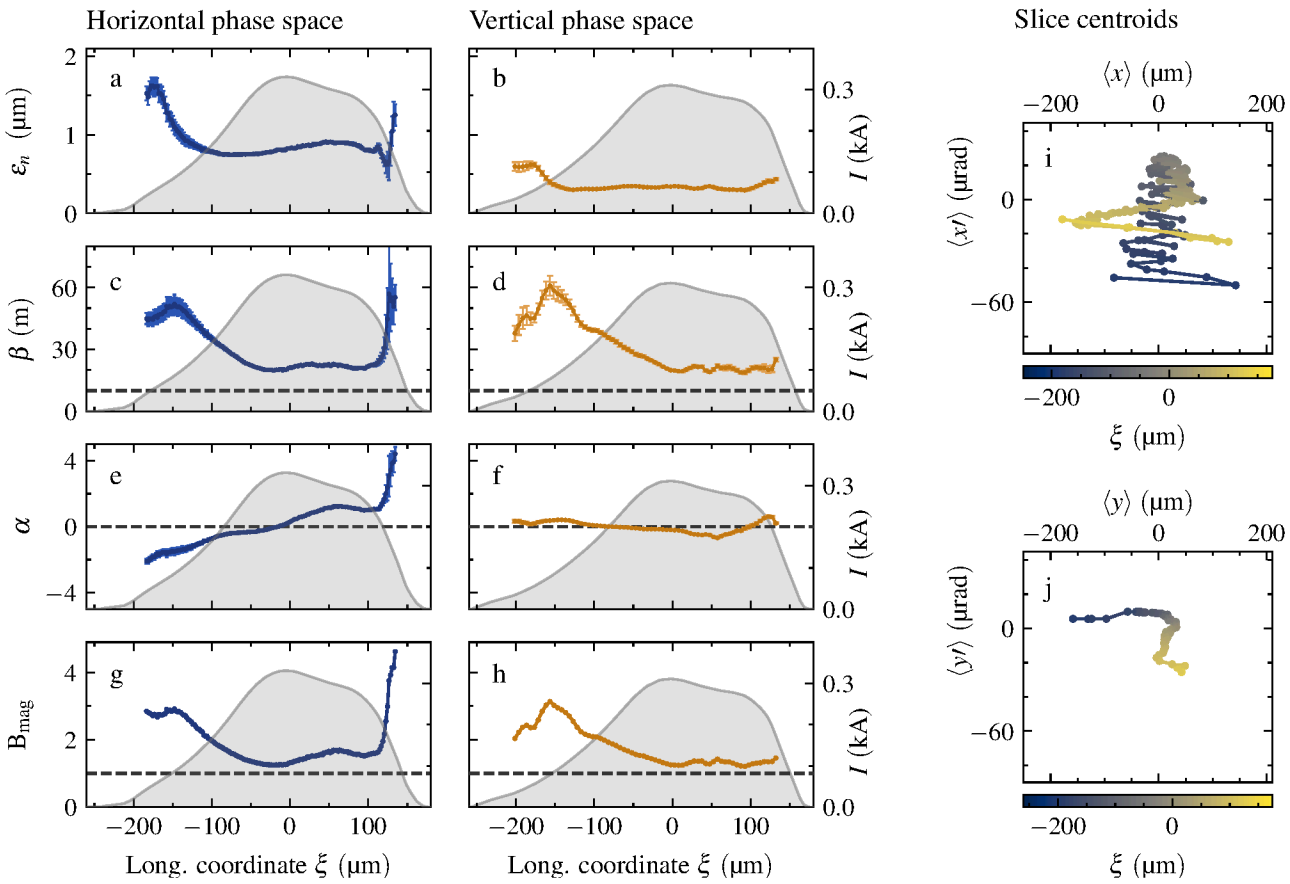

FIG. 7. Slice-emittance measurements in x and y, including: a–b) the normalised slice emittance; c–d) the beta function β at the reference point; e–f) the alpha parameter α at the reference point; g–h) the mismatch parameter B_{mag}; and i–j) the slice centroids, respectively. See text for details.

$\beta_x = \beta_y = 10$ m and $\alpha_x = \alpha_y = 0$. The design optic downstream of that point is optimised to obtain Courant-Snyder parameters in the streaking direction equal to $\beta_{TDS} = 100$ m and $\alpha_{TDS} = 0$ at the location of the TDS, while simultaneously achieving parallel-to-point imaging conditions between the TDS and the screen. In the axis perpendicular to the streak, the phase advance between the reference point and the screen is scanned in 10 steps within a range of $\Delta\mu = 180$ deg, with the beta function at the screen fixed to $\beta_{scr} \approx 25$ m—which, for an expected normalised emittance of $\varepsilon_{x,n} \approx 1$ µm, results in a beam size of $\sigma_{x,\beta} \approx 130$ µm, well above the screen resolution. Since the Courant-Snyder parameters at the reference point are the same in x and y, the measurement of the vertical slice emittance only requires inverting the polarity of the quadrupoles and switching the streaking direction from vertical to horizontal.

The shear parameter is measured at each zero crossing at the beginning of the scans. The unstreaked beam size, in contrast, is measured at each scan step and the largest value is used to calculate an upper bound of the longitudinal resolution according to Eq. (6). For vertical streaking, the obtained shear parameter is $S_y = 25.39 \pm 0.01$ and the natural (unstreaked) beam size $\sigma_{y,\beta} = 85 \pm 1$ µm, which result in a longitudinal resolution of $R_\xi = 3.4$ µm (11.2 fs). For the horizontal one, $S_y = 20.95 \pm 0.01$ and $\sigma_{x,\beta} = 162 \pm 2$ µm, which result in a resolution of $R_\xi = 7.7$ µm (25.8 fs). At each scan step 25 beam images are collected. The median of the background is substracted from the images, which are then analysed in slices perpendicular to the streak with a width corresponding to the calculated resolution. For each slice, the transverse beam size is obtained by fitting a Gaussian function to its projection and the emittance is calculated from the beam-transport equations by means of a least-squares fit as described in reference [65]. At each scan step, the TDS is operated at both zero crossings to be able to retrieve the intrinsic bunch correlations at the location of the screen and to invert the non-linear mapping $\mu : \xi \mapsto y$ (cf. Section II B). This allows both to reconstruct the current profile and to adjust the longitudinal coordinate of each slice to its undistorted value, which also enables a consistent comparison of the sliced beam parameters measured at each of the two zero crossings.

The results of the two scans are shown in Fig. 7, includ-

ing the normalised slice emittance ε_n, the beta β and alpha α functions at the reconstruction plane, their corresponding mismatch parameter B_{mag} [65], and the slice centroids. The current profile is shown in the background of Figs. 7(a–h). At the initial and final steps of the scans, up to ≈ 10 % of the charge was lost, which partly accounts for the differences in current profile between the horizontal and vertical phase space, most noticeably at the head and tail of the bunch. To a lesser degree, these differences can also be attributed to the different resolution achieved along the bunch for each streaking direction. Even though these differences introduce an additional uncertainty to the measured r.m.s. bunch duration—$\sigma_\xi = 80 \pm 4$ µm (268 ± 13 fs) for vertical streaking and $\sigma_\xi = 86 \pm 3$ µm (287 ± 9 fs) for the horizontal one—they do not represent a serious drawback to the illustrative purpose of these measurements, which still provide a detailed insight into the time-resolved phase space of the particle distribution that reveals clear differences between the beam dynamics in each of the two transverse planes. The core horizontal normalised slice emittance is $\varepsilon_{x,n} = 0.83 \pm 0.01$ µm, whereas the vertical one is $\varepsilon_{y,n} = 0.34 \pm 0.01$ µm. This difference is most probably due to coherent-synchrotron-radiation (CSR) effects that arise in the horizontal dipoles along the beamline, since both the bunch compression and most of the extraction from the linac take place in the horizontal plane. The disagreement between the measured and the design Courant-Snyder parameters is reflected in the value of the mismatch parameter, which is only close to $B_{mag} \approx 1$ around the central slice, since this is the region that was nearly matched during the beamline setup. Nonetheless, an error analysis based on computer simulations (cf. Appendix) indicates that the measurement is not particularly sensitive to B_{mag} and, in the region -100 µm $\lesssim \xi \lesssim 100$ µm, the emittance error is around or below 5 %. The slice centroids in both planes exhibit a rather complex structure, which hints the presence of collective effects arising at different locations along the bunch.

For the longitudinal-phase-space measurement, the beam parameters in the vertical (streaking) direction at the location of the TDS are the same as for the slice-emittance scans—i.e., $\beta_{y,\mathrm{TDS}} = 100$ m and $\alpha_{y,\mathrm{TDS}} = 0.0$—and the magnet lattice between the TDS and the second screen is adjusted to fulfill parallel-to-point imaging conditions in the vertical direction, while optimising the energy resolution in the horizontal (cf. Section II C). The unstreaked beam size measured at the screen is $\sigma_{y,\beta} = 63.3 \pm 0.5$ µm and the shear parameter $S_y = 47.72 \pm 0.02$, which result in a longitudinal resolution of $R_\xi = 1.3$ µm (4.4 fs). The energy resolution is not directly measured but is estimated by means of Eq. (17) using the beam parameters obtained in the horizontal slice-emittance measurement. The core slice emittance was found to be $\varepsilon_{x,n} = 0.83 \pm 0.01$ µm and the beta function is calculated by transporting the Courant-Snyder parameters from the reference point to the longitudinal-phase-space screen $\beta_{x,\mathrm{scr}} = 2.19 \pm 0.07$ m. By performing a dipole-current scan, the dispersion at the screen is found to be $D_x = 256 \pm 1$ mm. With these parameters, the energy resolution of the measurement at the core of the bunch is $R_\delta = 1.4 \cdot 10^{-4}$. The spatial resolution of the screen (cf. Section III C) translates into an energy resolution of $R_{\mathrm{scr}} \cdot D_x^{-1} = 3.9 \cdot 10^{-5}$.

The longitudinal-phase-space density measured at each zero crossing is shown in Fig. 8, in which the most prominent differences observed between the two are slice-mean-energy shifts along the energy axis that have a strong impact on the overall shape of the bunch. This is clearly reflected in the energy distribution shown in Figs. 8(a) and 8(c). As mentioned in Section II C, such differences originate from intrinsic correlations between the longitudinal ξ and both transverse coordinates y and y', so that different slices gain or lose different amounts of energy as the bunch propagates through the TDS according to Eq. (12). In the longitudinal axis, in contrast, the slice rms energy spread σ_δ and the current profile I exhibit only minor differences between the two zero crossings, which is the result of the good resolution achieved, i.e., the extent of the natural (unstreaked) beam size—and, accordingly, the extent of the intrinsic bunch correlations at the screen—is much smaller than the streaked beam size.

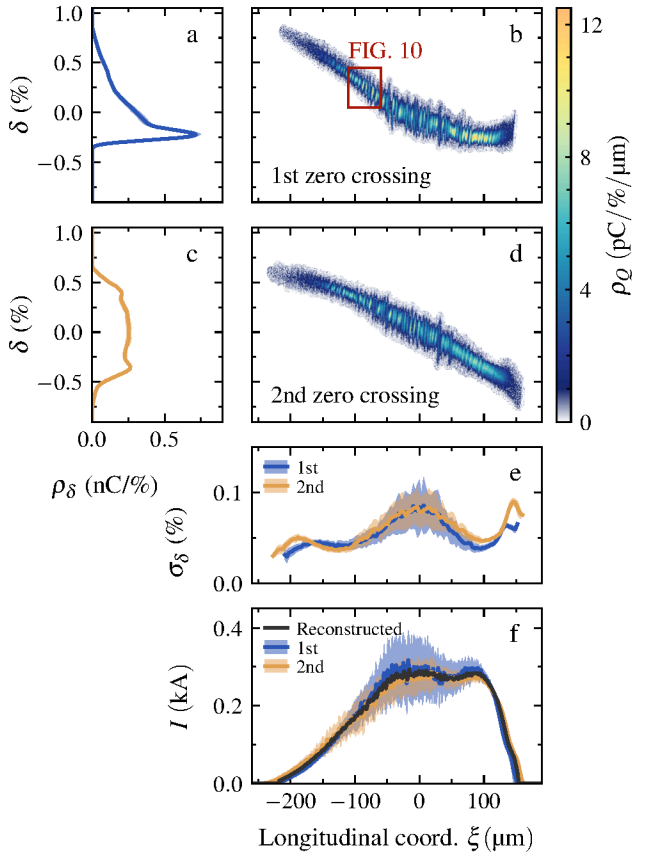

FIG. 8. Longitudinal-phase-space measurement at the 1st and 2nd zero crossing, including: (a, c) averaged projected energy distribution; (b, d) sample images; (e) averaged slice rms energy spread; (f) averaged current profiles and current profile reconstructed by means of the two-point-tomographic reconstruction. The region inside the inlet inserted in the sample image shown in (c) is analysed in more detail Fig. 10.

In order to reconstruct the "true" longitudinal-phase-space

density, the following procedure is applied. Firstly, the non-linear mapping of the TDS $\mu : \xi \mapsto y$ is computed by means of the two-point tomographic reconstruction and the longitudinal coordinate of each slice is adjusted to its undistorted value. In this way, the slice parameters measured at each of the zero crossings can be compared to each other consistently. Secondly, the slice relative mean energy deviation is retrieved by means of Eq. (13). Finally, the induced slice energy spread σ_{IES} is calculated according to Eq. (14) by propagating the slice Courant-Snyder parameters from the reference point to the entrance of the TDS. At the core of the bunch $\sigma_{\mathrm{IES}} = (3.11 \pm 0.02) \cdot 10^{-4}$. The obtained values are subsequently substracted in quadrature from the measured slice energy spread together with both the energy and the screen resolution according to Eq. (18). The measured slice energy spread at the core of the bunch is $\sigma_{\delta,\mathrm{meas}} = (8.4 \pm 0.3) \cdot 10^{-4}$. After substraction of the different contributions, the "true" slice energy spread becomes $\sigma_{\delta,0} = (7.7 \pm 0.7) \cdot 10^{-4}$. Together with the time-resolved transverse phase space obtained from the slice-emittence measurements in x and y, the reconstructed longitudinal-phase-space density can be used to reproduce the particle distribution at the reference point of the emittance measurements. To that end the obtained first and second moments of each slice (cf. Eq. (30)) are used to generate random particles following a bivariate Gaussian distribution, the number of particles being proportinal to the beam current at the location of the slice. The result is shown in Fig. 9, with the longitudinal phase space at the top and the spatial charge distribution in x and y at the bottom. Such a time-resolved phase-space reconstruction constitutes an exceptional tool to, e.g., benchmark start-to-end simulations and understand the beam dynamics along the machine.

A clear sign of the resolution power of the PolariX-TDS is the observation in Fig. 8 of the longitudinal substructure resulting from microbunching instabilities [18, 91]. An analysis of the size of these microbunches suggests the actual resolution achieved in the measurement. This is shown in Fig. 10. The top plot reproduces the region of the longitudinal-phase-space density highlighted in Fig. 8(b), whereas the bottom one shows an energy slice together with a Gaussian function fitted to a single microbunch. The obtained sigma $\sigma_\xi = 0.98 \pm 0.03$ µm (3.3 ± 0.1 fs) represents an improvement of 25 % with respect to the longitudinal resolution calculated from the projected beam size, which becomes larger due to the intrinsic bunch correlations. From the vertical slice-emittance measurement and the transport of the obtained Courant-Snyder parameters from the reference point to the longitudinal-phase-space screen, it is possible to compute the local resolution along the bunch and estimate its value at the location of the microbunch $\xi = -83.8$ µm. With a normalised emittance of $\varepsilon_{y,n} = 0.32 \pm 0.01$ µm, a beta function at the screen of $\beta_{y,\mathrm{scr}} = 10.6 \pm 0.2$ m, and a measured shear parameter of $S_y = 47.72 \pm 0.02$, the resolution is $R_\xi = 1.01 \pm 0.03$ µm (3.3 ± 0.1 fs), in very good agreement with the value obtained from the image analysis performed here.

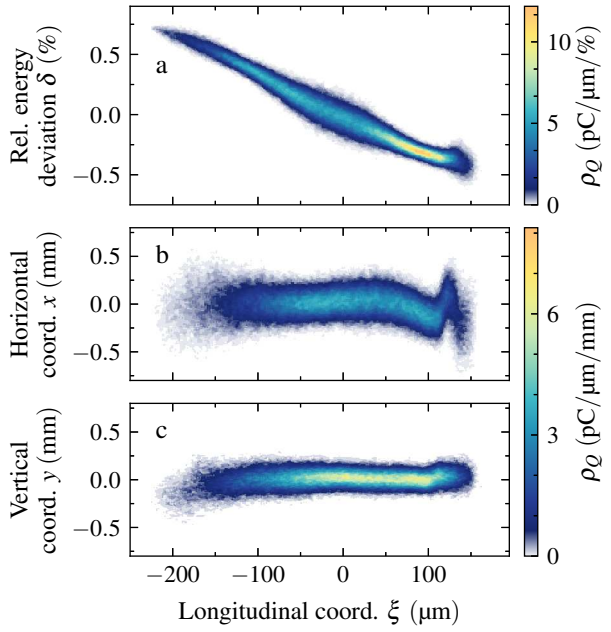

FIG. 9. Time-resolved phase space reconstruction of the bunch at the reference point of the slice-emittance measurement, including: (a) longitudinal-phase-space density and (b, c) spatial charge distribution in ξ–x and ξ–y, respectively, in which the centroid offsets at the head of the bunch originating from CSR effects can be clearly observed.

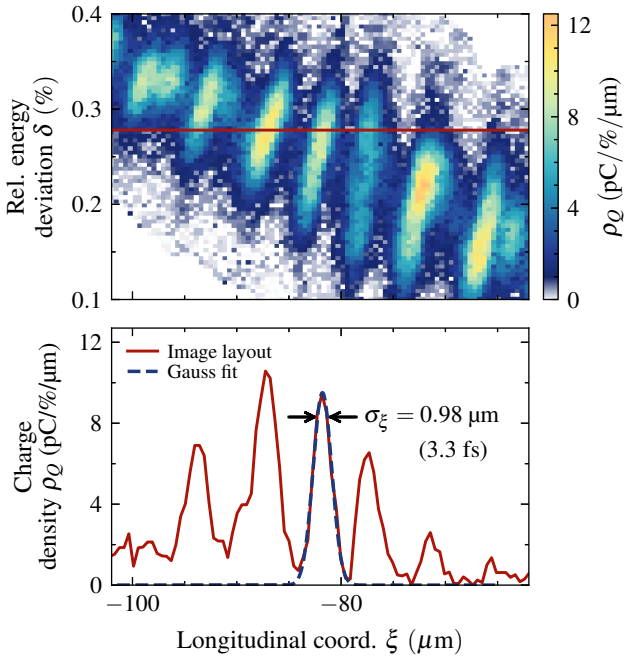

FIG. 10. Effective (local) longitudinal resolution determined by analysing the structure size of the micro-bunching instabilities. Top: longitudinal-phase-space density of the inspected region. The analysed lineout is indicated with a red line. Bottom: lineout of the top image (red line) with a Gaussian fit applied to a selected microbunch (blue dashed line) demonstrating a resolution of at least $R_\xi = 3.3 \pm 0.1$ fs.

The capability of the PolariX-TDS to diagnose both transverse planes also allows to assess of the impact of longitudinal-phase-space shearing effects on the measurement as described by Eq. (19). From the reconstructed time-resolved phase space, the terms of the covariance matrix given in Eq. (30) at the TDS entrance are now known, which can be transported to the screen by simple matrix multiplication to obtain the Pearson coefficient and the geometric tilt of each longitudinal slice. The results of the calculation are shown in Fig. 11. For most of the longitudinal extent of the bunch the Pearson coefficient is around or above $\rho_{x,y} \approx -0.1$, which can be considered negligible, and only at the very front its value becomes considerable. However the angle of the tilt is kept at pretty moderate values above $\theta_{x,y} > -4$ deg (i.e., slightly rotated to the right) and in a broad region around the core of the bunch it is almost 0 deg. The practical absence of longitudinal-phase-space distortions in the measurement would allow, for instance, to perform a detailed analysis of the observed micro-bunching instabilities.

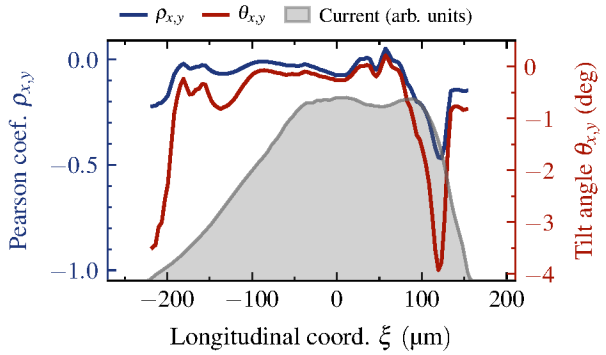

FIG. 11. Impact of longitudinal-phase-space shearing effects induced by the TDS, characterised by the Pearson coefficient of the beam matrix in the transverse plane $\rho_{x,y}$ (left axis, blue) and the geometric tilt $\theta_{x,y}$ (right axis, red) of each longitudinal slice. The values obtained indicate a negligible impact of shearing effects on the measurement.

VI. CONCLUSION

A comprehensive beam-based commissioning campaign has been conducted to validate the operation of the PolariX-TDS prototype, an advanced X-band transverse-deflection RF structure system with the new feature of providing a variable polarization of the deflecting force [40, 52, 53]. The novel device has been developed and produced within the frame of a collaboration between DESY, PSI, and CERN. Two sets of measurements have been carried out to assess: 1) the RF performance of the system and 2) its diagnostic capabilities.

The variable phase shifter works as expected and provides full flexibility to adjust the transverse direction of the streaking field. The measurements show a slight power imbalance between the two inputs of the E-rotator, which receive 55 % and 45 % of the total power sent into the structure. When operating at the zero crossing, this imbalance results in a net deflection in the direction perpendicular to the streak. For the prototype, this behaviour can be compensated with beam steerer and it should be carefully accounted for in the future installation of other PolariX-TDS setups. The measured power-to-voltage constant $D = 5.1 \pm 0.1$ MV/$\sqrt{\text{MW}}$ exhibits an excellent agreement with its nominal value $D = 5.2$ MV/$\sqrt{\text{MW}}$ [52], which validates the high-precision machining achieved in the production of the device. Finally, the good RF performance of the whole setup—including the synchronsation system at FLASH—enables an assessment of the stability of the arrival-time of the bunches delivered by FLASH with a precision better than 10 fs and the bunch-duration stability with a precision on the order 0.1%.

With regards to the unique diagnostic capabilities of the PolariX-TDS, a time-resolved phase-space reconstruction of an electron bunch has been accomplished, which is based on the independent measurement of the slice emittance in both x and y, and the longitudinal phase space. The level of detail achieved in the longitudinal-phase-space screen, has enabled to measure the structure size of microbunching instabilities with a sigma as low as $\sigma_\xi = 3.3 \pm 0.1$ fs, in excellent agreement with both the local longitudinal resolution retrieved from the slice-emittance measurements and the expected performance of the system. The ability of the new device to access the slice transverse beam parameters in the direction of the streaking field, enables the experimental validation of second-order TDS-induced effects expected from theoretical predictions, including the magnitude of slice mean energy shifts in the energy axis and the impact of longitudinal-phase-space shearing effects.

In summary, the PolariX-TDS system has been successfully commissioned and its outstanding performance has been validated by means of beam-based measurements. The novel device provides a detailed insight into the phase-space structure of electron bunches with a resolution on the femtosecond time scale, which allows to investigate the beam dynamics along the machine in the full transverse plane. Additionally, a new analysis that accounts for TDS-induced effects is now possible and will be developed in the future for demanding diagnostic applications.

ACKNOWLEDGMENTS

The authors would like to thank the FLASH team, the FLASH operators, and the DESY technical groups for their support during the installation and commissioning of the PolariX-TDS system and its beamline. We are also thankful to S. Karstensen, K. Ludwig, F. Marutzky, A. Rahali, A. Schleiermacher and S. Thiele, as well as the FLASHForward team for their scientific and technical support. We especially thank Bolko Beutner for fruitful discussions on the operation of the TDS and the data analysis, Carl A. Lindstrøm for discussions on beam dynamics and lattice optics, and Johann Zemella for his support during the commissioning of the PolariX-TDS beamline. We acknowledge support from

DESY (Hamburg, Germany), a member of the Helmholtz Association HGF.

APPENDIX: EMITTANCE-MEASUREMENT ERRORS

The design parameters of the slice-emittance measurement depend on the initial Courant-Snyder parameters at the reference point. Therefore, if the beam is not well matched at that position, the actual phase-advance range covered in the scan will deviate from the optimal case shown in Fig. 7a. To assess the sensitivity of the measurement to the mismatch, simulations are performed for a range of initial beam parameters enclosing those observed in the experiments. For each virtual measurement, 1100 random seeds are generated and a relative beam size error of 5 % following a Gaussian distribution is assumed. The relative emittance error obtained from the χ^2 fit [65] is shown in Fig. 12 together with contour lines indicating the corresponding values of the mismatch parameter. The color scale in the plot is limited to 15 % to better appreciate the error around the matched solution (white dot). For most of the slices the mismatch parameter is below $B_{mag} < 2.5$ (cf. Fig. 7b), which results in emittance errors of around 5 % down to a minimum of 2.9 %.

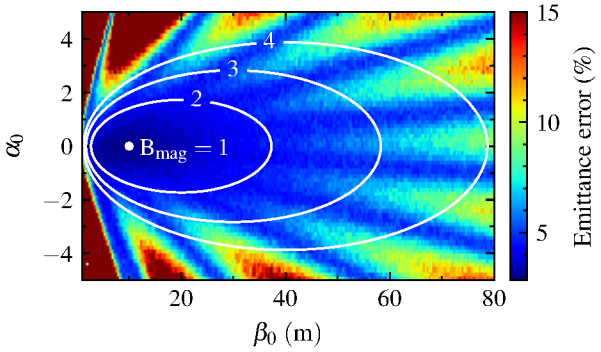

FIG. 12. Relative emittance error for different initial beam parameters β_0 and α_0 at the reference point of the measurement. The matched solution is indicated with a white dot and several contour lines indicate mismatch parameters of $B_{mag} = 2$, 3 and 4.

[1] W. Ackermann, G. Asova, V. Ayvazyan, A. Azima, N. Baboi, J. Bähr, V. Balandin, B. Beutner, A. Brandt, and A. Bolzmann *et al.*, Operation of a free-electron laser from the extreme ultraviolet to the water window, Nature Photonics **1**, 336 (2007).

[2] P. Emma, R. Akre, J. Arthur, R. Bionta, C. Bostedt, J. Bozek, A. Brachmann, P. Bucksbaum, R. Coffee, and F.-J. Decker *et al.*, First lasing and operation of an ångstrom-wavelength free-electron laser, Nature Photonics **4**, 641 (2010).

[3] H. Tanaka, M. Yabashi, H. Aoyagi, T. Asaka, Y. Asano, N. Azumi, T. Bizen, H. Ego, K. Fukami, and T. Fukui *et al.*, A compact X-ray free-electron laser emitting in the sub-ångström region, Nature Photonics **6**, 540 (2012).

[4] E. Allaria, R. Appio, L. Badano, W. A. Barletta, S. Bassanese, S. G. Biedron, A. Borga, E. Busetto, D. Castronovo, and P. Cinquegrana *et al.*, Highly coherent and stable pulses from the FERMI seeded free-electron laser in the extreme ultraviolet, Nature Photonics **6**, 699 (2012).

[5] W. Decking, S. Abeghyan, P. Abramian, A. Abramsky, A. Aguirre, C. Albrecht, P. Alou, M. Altarelli, P. Altmann, and K. Amyan *et al.*, A MHz-repetition-rate hard X-ray free-electron laser driven by a superconducting linear accelerator, Nature Photonics **14**, 391 (2020).

[6] E. Prat, R. Abela, M. Aiba, A. Alarcon, J. Alex, Y. Arbelo, C. Arrell, V. Arsov, C. Bacellar, and C. Beard *et al.*, A compact and cost-effective hard X-ray free-electron laser driven by a high-brightness and low-energy electron beam, Nature Photonics **14**, 748 (2020).

[7] T. Bredtmann, M. Ivanov, and G. Dixit, X-ray imaging of chemically active valence electrons during a pericyclic reaction, Nature Communications **5**, 1 (2014).

[8] S. H. Park, A. Katoch, K. H. Chae, S. Gautam, P. Miedema, S. W. Cho, M. Kim, R. P. Wang, M. Lazemi, F. de Groot, and S. Kwon, Direct and real-time observation of hole transport dynamics in anatase TiO2 using X-ray free-electron laser, Nature Communications **13**, 2 (2022).

[9] G. Kastirke, F. Ota, D. V. Rezvan, M. S. Schöffler, M. Weller, J. Rist, R. Boll, N. Anders, T. M. Baumann, and S. Eckart *et al.*, Investigating charge-up and fragmentation dynamics of oxygen molecules after interaction with strong X-ray free-electron laser pulses, Physical Chemistry Chemical Physics **24**, 27121 (2022).

[10] J. M. Madey, Stimulated emission of bremsstrahlung in a periodic magnetic field, Journal of Applied Physics **42**, 1906 (1971).

[11] A. M. Kondratenko and E. L. Saldin, Generation of Coherent Radiation by a Relativistic Electron Beam in an Ondulator, Particle Accelerators **10**, 207 (1980).

[12] E. L. Saldin, E. A. Schneidmiller, and M. V. Yurkov, *The Physics of Free Electron Lasers* (Springer-Verlag Berlin Heidelberg GmbH, 2013).

[13] L. H. Yu, Generation of intense uv radiation by subharmonically seeded single-pass free-electron lasers, Physical Review A **44**, 5178 (1991).

[14] L. H. Yu, M. Babzien, L. F. Dimauro, A. Doyuran, W. Graves, E. Johnson, S. Krinsky, R. Malone, I. Pogorelsky, and J. Skaritka *et al.*, High-Gain Harmonic-Generation Free-Electron Laser, Science **289**, 932 (2000).

[15] G. Stupakov, Using the beam-echo effect for generation of short-wavelength radiation, Physical Review Letters **102**, 10.1103/PhysRevLett.102.074801 (2009).

[16] E. L. Saldin, E. A. Schneidmiller, and M. V. Yurkov, On the Coherent Radiation of an Electron Bunch Moving in an Arc of a Circle, Nuclear Instruments and Methods in Physics Research, Section A: Accelerators, Spectrometers, Detectors and Associated Equipment **398**, 373 (1997).

[17] M. Borland, Y. Chae, S. Milton, R. Soliday, P. Emma, P. Krejcik, C. Limborg, H. Nuhn, and M. Woodley, Start-to-end Jitter Simulations of the Linac Coherent Light Source, in *Particle Accelerator Conference* (Chicago, Illinois, USA, 2001) pp. 2707–2709.

[18] E. L. Saldin, E. A. Schneidmiller, and M. V. Yurkov, Longitudinal space charge-driven microbunching instability in the TESLA Test Facility linac, Nuclear Instruments and Methods in Physics Research, Section A: Accelerators, Spectrometers, Detectors and Associated Equipment **528**, 355 (2004).

[19] P. Chen, J. M. Dawson, R. W. Huff, and T. Katsouleas, Acceleration of Electrons by the Interaction of a Bunched Electron Beam with a Plasma, Physical Review Letters **54**, 693 (1985).

[20] R. D. Ruth, A. Chao, P. L. Morton, and P. B. Wilson, A Plasma Wake Field Accelerator, Particle Accelerators **17**, 171 (1985).

[21] D. H. Whittum, W. M. Sharp, S. S. Yu, M. Lampe, and G. Joyce, Electron-hose instability in the ion-focused regime, Physical Review Letters **67**, 991 (1991).

[22] C. A. Lindstrøm, E. Adli, J. Pfingstner, E. Marin, and D. Schulte, Transverse tolerances of a multi-stage plasma wakefield accelerator, in *Proceedings of the 7th International Particle Accelerator Conference - IPAC2016* (JACoW Publishing, Busan, Korea, 2016) pp. 2561–2564.

[23] C. A. Lindstrøm, Staging of plasma-wakefield accelerators, Physical Review Accelerators and Beams **24**, 14801 (2021).

[24] O. H. Altenmueller, R. R. Larsen, and G. A. Loew, Investigations of Traveling-Wave Separators for the Stanford Two-mile Linear Accelerator, Review of Scientific Instruments **35**, 438 (1964).

[25] I. Ben-Zvi, J. X. Qiu, and X. Wang, Picosecond-Resolution Slice' Emittance Measurement of Electron-Bunches, in *Proceedings of the 8th Particle Accelerator Conference* (1998) pp. 1971–1975.

[26] P. Emma, J. Frisch, and P. Krejcik, *SLAC Report No. LCLS-TN-00-12*, Tech. Rep. (SLAC, Stanford, CA, USA, 2000).

[27] R. Akre, L. Bentson, P. Emma, and P. Krejcik, *Particle Accelerator Conference*, Tech. Rep. (Chicago, Illinois, USA, 2001).

[28] D. Alesini, G. Di Pirro, L. Ficcadenti, A. Mostacci, L. Palumbo, J. B. Rosenzweig, and C. Vaccarezza, RF deflector design and measurements for the longitudinal and transverse phase space characterization at SPARC, Nuclear Instruments and Methods in Physics Research, Section A: Accelerators, Spectrometers, Detectors and Associated Equipment **568**, 488 (2006).

[29] M. Röhrs, C. Gerth, H. Schlarb, B. Schmidt, and P. Schmüser, Time-resolved electron beam phase space tomography at a soft x-ray free-electron laser, Physical Review Special Topics: Accelerators and Beams **12**, 050704 (2009).

[30] P. Craievich, M. Petronio, S. G. Biedron, D. Castronovo, M. Dal Forno, S. Di Mitri, N. Faure, D. La Civita, G. Penco, L. Rumiz, L. Sturari, R. Vescovo, and D. Wang, Implementation of radio-frequency deflecting devices for comprehensive high-energy electron beam diagnosis, IEEE Transactions on Nuclear Science **62**, 210 (2015).

[31] H. Ego, H. Maesaka, T. Sakurai, Y. Otake, T. Hashirano, and S. Miura, Transverse C-band deflecting structure for longitudinal electron-bunch-diagnosis in XFEL "sACLA", Nuclear Instruments and Methods in Physics Research, Section A: Accelerators, Spectrometers, Detectors and Associated Equipment **795**, 381 (2015).

[32] Y. Ding, A. Brachmann, F. J. Decker, D. Dowell, P. Emma, J. Frisch, S. Gilevich, G. Hays, P. Hering, and Z. Huang *et al.*, Measurements and simulations of ultralow emittance and ultrashort electron beams in the linac coherent light source, Physical Review Letters **102**, 5 (2009).

[33] J. W. Wang and S. Tantawi, X-band traveling wave RF deflector structures, in *Proceedings of the 24th Linear Accelerator Conference* (JACoW Publishing, 2009) pp. 966–968.

[34] Y. Ding, C. Behrens, P. Emma, J. Frisch, Z. Huang, H. Loos, P. Krejcik, and M. H. Wang, Femtosecond x-ray pulse temporal characterization in free-electron lasers using a transverse deflector, Physical Review Special Topics - Accelerators and Beams **14**, 120701 (2011).

[35] P. Krejcik, F.-J. Decker, Y. Ding, J. Frisch, and Z. Huang, Commissioning the new LCLS X-Band Transverse Deflecting Cavity with Femtosecond Resolution, in *Proceedings of the 2nd International Beam Instrumentation Conference - IBIC2013* (JACoW Publishing, Oxford, UK, 2013) pp. 308–311.

[36] V. A. Dolgashev, G. Bowden, Y. Ding, P. Emma, P. Krejcik, J. Lewandowski, C. Limborg, M. Litos, J. Wang, and D. Xiang, Design and application of multimegawatt X-band deflectors for femtosecond electron beam diagnostics, Physical Review Special Topics - Accelerators and Beams **17**, 102801 (2014).

[37] C. Behrens, F.-J. Decker, Y. Ding, V. A. Dolgashev, J. Frisch, Z. Huang, P. Krejcik, H. Loos, A. Lutman, and T. J. Maxwell *et al.*, Few-femtosecond time-resolved measurements of X-ray free-electron lasers, Nature Communications **5** (2014).

[38] E. Prat, A. Malyzhenkov, and P. Craievich, Sub-femtosecond time-resolved measurements of electron bunches with a C-band radio-frequency deflector in x-ray free-electron lasers, Review of Scientific Instruments **94**, 10.1063/5.0144876 (2023).

[39] M. Aicheler, P. Burrows, M. Draper, T. Garvey, P. Lebrun, K. Peach, N. Phinney, H. Schmickler, D. Schulte, and N. Toge, *A Multi-TeV Linear Collider Based on CLIC Technology*, Tech. Rep. (CERN, Geneva, Switzerland, 2012).

[40] A. Grudiev, *Design of compact high power RF components at X-band*, Tech. Rep. (CERN, Geneva, Switzerland, 2016).

[41] U. Ellenberger, L. Paly, H. Blumer, C. Zumbach, F. Loehl, M. Bopp, and H. Fitze, Status of the manufacturing process for the SwissFEL c-band accelerating structures, in *Proceedings of the 35th Free-Electron Laser Conference - FEL2013* (JACoW Publishing, New York, NY, USA, 2013) pp. 245–249.

[42] R. Zennaro, J. Alex, A. Citterio, and J.-Y. Raguin, Measurements and High-power Test of the First C-Band Accelerating Structure for SwissFEL, in *Proceedings of the 27th Linear Accelerator Conference - LINAC2014* (JACoW Publishing, Geneva, Switzerland, 2014) pp. 333–335.

[43] A. Aschikhin, C. Behrens, S. Bohlen, J. Dale, N. M. Delbos, L. Di Lucchio, E. Elsen, J. H. Erbe, M. Felber, and B. Foster *et al.*, The FLASHForward facility at DESY, Nuclear Instruments and Methods in Physics Research, Section A: Accelerators, Spectrometers, Detectors and Associated Equipment **806**, 175 (2016).

[44] R. D'Arcy, A. Aschikhin, S. Bohlen, G. J. Boyle, T. Brümmer, J. Chappell, S. Diederichs, B. Foster, M. J. Garland, and L. Goldberg *et al.*, FLASHForward: Plasma wakefield accelerator science for high-average-power applications, Philosophical Transactions of the Royal Society A: Mathematical, Physical and Engineering Sciences **377** (2019).

[45] B. Faatz, E. Plönjes, S. Ackermann, A. Agababyan, V. Asgekar, V. Ayvazyan, S. Baark, N. Baboi, V. Balandin, and N. von Bargen *et al.*, Simultaneous operation of two soft x-ray free-electron lasers driven by one linear accelerator, New Journal of Physics **18**, 62002 (2016).

[46] F. Burkart, R. W. Assmann, H. Dinter, S. Jaster-Merz, W. Kuropka, F. Mayet, B. Stacey, and T. Vinatier, The ARES Linac at DESY, in *Proceedings of LINAC2022* (JACoW Publishing, Liverpool, UK, 2022) pp. 691–694.

[47] R. Ganter, R. Abela, A. Alarcon, J. Alex, C. Arrell, V. Arsov, S. Bettoni, M. Bopp, C. Bostedt, and H. H. Braun *et al.*, The SwissFEL soft X-ray free-electron laser beamline: Athos, Journal of Synchrotron Radiation **26**, 1073 (2019).

[48] B. Marchetti, R. Assmann, B. Beutner, J. Branlard, F. Christie, R. D'Arcy, W. Decking, U. Dorda, J. Herrmann, and M. Hoffmann *et al.*, X-Band TDS Project, in *Proceedings of the 8th International Particle Accelerator Conference - IPAC2017* (JACoW Publishing, Copenhagen, Denmark, 2017) pp. 184–187.

[49] P. Craievich, M. Bopp, H. Braun, R. Ganter, T. Kleeb, M. Pedrozzi, E. Prat, S. Reiche, R. Zennaro, and A. Grudiev *et al.*,

Status of the PolariX-TDS Project, in *Proceedings of the 9th International Particle Accelerator Conference - IPAC2018* (JACoW Publishing, Vancouver, BC, Canada, 2018) pp. 3808–3811.

[50] P. Craievich, M. Bopp, H. Braun, A. Citterio, R. Ganter, F. Marcellini, T. Kleeb, M. Pedrozzi, E. Prat, and S. Reiche *et al.*, The PolariX-TDS Project: Bead-pull Measurements and High-power Test on the Prototype, in *Proceedings of the 39th Free-Electron Laser Conference - FEL2019* (JACoW Publishing, Hamburg, Germany, 2019) pp. 396–399.

[51] D. Marx, R. W. Assmann, P. Craievich, K. Floettmann, A. Grudiev, and B. Marchetti, Simulation studies for characterizing ultrashort bunches using novel polarizable X-band transverse deflection structures, Scientific Reports **9**, 1 (2019).

[52] P. Craievich, M. Bopp, H. H. Braun, A. Citterio, R. Fortunati, R. Ganter, T. Kleeb, F. Marcellini, M. Pedrozzi, and E. Prat *et al.*, Novel X-band transverse deflection structure with variable polarization, Physical Review Accelerators and Beams **23**, 112001 (2020).

[53] B. Marchetti, A. Grudiev, P. Craievich, R. Assmann, H. H. Braun, N. Catalan Lasheras, F. Christie, R. D'Arcy, R. Fortunati, and R. Ganter *et al.*, Experimental demonstration of novel beam characterization using a polarizable X-band transverse deflection structure, Scientific Reports **11**, 1 (2021).

[54] S. M. Jaster-Merz, R. W. Assmann, J. Beinortaite, J. Björklund Svensson, R. Brinkmann, F. Burkart, R. D'Arcy, H. Dinter, P. Gonzalez Caminal, and A. L. Kanekar *et al.*, 5D Phase-Space Reconstruction of an Electron Beam, in *Proceedings of the 14th International Particle Accelerator Conference - IPAC2023* (JACoW Publishing, Venezia, Italy, 2023) pp. 1616–1619.

[55] S. M. Jaster-Merz, R. W. Assmann, R. Brinkmann, F. Burkart, W. Hillert, M. Stanitzki, and T. Vinatier, 5D tomographic phase-space reconstruction of particle bunches (2023), arXiv:2305.03538.

[56] S. Schreiber and B. Faatz, The free-electron laser FLASH, High Power Laser Science and Engineering **3** (2015).

[57] H. Hahn, Deflecting Mode in Circular Iris-Loaded Waveguides, Review of Scientific Instruments **34**, 1094 (1963).

[58] V. V. Paramonov and K. Floettmann, *Fundamental characteristics of transverse deflecting fields*, Tech. Rep. (DESY, Hamburg (Germany), 2018).

[59] T. P. Wangler, *RF Linear Accelerators*, 2nd ed. (WILEY-VCH Verlag GmbH & Co. KGaA, Weinheim, Germany, 2008).

[60] E. Courant and H. Snyder, Theory of the alternating-gradient synchrotron, Annals of Physics **3**, 1 (1958).

[61] P. Dijkstal, *Temporal FEL Pulse Shaping and Diagnostics at SwissFEL with Tilted Electron Beams*, Ph.D. thesis, ETH Zürich (2022).

[62] K. L. Brown, *A First- and Second-Order Matrix Theory for the Design of Beam Transport Systems and Charged Particle Spectrometers*, Tech. Rep. (SLAC, Stanford, CA, USA, 1982).

[63] R. Akre, L. Bentson, and P. Emma, *SLAC*, Tech. Rep. May (SLAC, Stanford CA 94309, USA, 2002).

[64] H. Loos, *SLAC*, Tech. Rep. (SLAC, Stanford, CA, USA).

[65] M. G. Minty and F. Zimmermann, *Measurement and Control of Charged Particle Beams* (Springer, Berlin, Heidelberg, New York, 2003).

[66] X. Qiu, K. Batchelor, I. Ben-Zvi, and X. J. Wang, Demonstration of emittance compensation through the measurement of the slice emittance of a 10-ps electron bunch, Physical Review Letters **76**, 3723 (1996).

[67] E. Prat, M. Aiba, S. Bettoni, B. Beutner, S. Reiche, and T. Schietinger, Emittance measurements and minimization at the SwissFEL Injector Test Facility, Physical Review Special Topics: Accelerators and Beams **17**, 9 (2014).

[68] D. Marx, *Characterization of Ultrashort Electron Bunches at the SINBAD-ARES Linac*, Ph.D. thesis, Universität Hamburg (2019).

[69] W. K. Panofsky and W. A. Wenzel, Some Considerations Concerning the Transverse Deflection of Charged Particles in Radio-Frequency Fields, Review of Scientific Instruments **27**, 967 (1956).

[70] M. Yan, *Online diagnostics of time-resolved electron beam properties with femtosecond resolution for X-ray FELs*, Ph.D. thesis, Universität Hamburg (2015).

[71] C. Behrens and C. Gerth, On the Limitations of Longitudinal Phase Space Measurements usign a Transverse Deflecting Structure, in *Proceedings of the 9th European Workshop on Beam Diagnostics and Instrumentation for Particle Accelerators - DIPAC09* (JACoW, Basel, Switzerland, 2009) p. 3.

[72] E. Prat, P. Dijkstal, E. Ferrari, A. Malyzhenkov, and S. Reiche, High-resolution dispersion-based measurement of the electron beam energy spread, Physical Review Accelerators and Beams **23**, 90701 (2020).

[73] S. Tomin, I. Zagorodnov, W. Decking, N. Golubeva, and M. Scholz, Accurate measurement of uncorrelated energy spread in electron beam, Physical Review Accelerators and Beams **24**, 64201 (2021).

[74] P. González Caminal, *Time-Resolved Phase-Space Characterisation of Plasma-Wakefield-Accelerated Electrons at FLASHForward*, Ph.D. thesis, Universität Hamburg (2022).

[75] J. Rossbach, J. R. Schneider, and W. Wurth, 10 years of pioneering X-ray science at the Free-Electron Laser FLASH at DESY, Physics Reports **808**, 1 (2019).

[76] S. Schreiber, S. Lederer, L. Monaco, D. Sertore, and P. Michelato, Update on the Lifetime of Cs2Te Cathodes Operated at the FLASH Facility, in *Proceedings of the 38th International Free Electron Laser Conference - FEL2017* (JACoW Publishing, Santa Fe, NM, USA, 2017) pp. 407–410.

[77] E. Vogel, C. Albrecht, N. Baboi, C. Behrens, T. Delfs, J. Eschke, C. Gerth, M. G. Hoffmann, M. Hoffmann, and M. Hüning *et al.*, Test and Commissioning of the Third Harmonic RF System for FLASH, in *Proceedings of the 1st International Particle Accelerator Conference - IPAC2010* (JACoW Publishing, Kyoto, Japan, 2010) pp. 4281–4283.

[78] F. Stulle, *A bunch compressor for small emittances and high peak currents at the VUV Free-Electron Laser*, Ph.D. thesis, Universität Hamburg (2004).

[79] M. Scholz, *Design of the Extraction Arc for the 2nd Beam Line of the Free-Electron Laser FLASH*, Ph.D. thesis, Universtität Hamburg (2013).

[80] C. Behrens, *Report on the design of the electron beamline of FLASHForward*, Tech. Rep. (DESY, Hamburg, Germany, 2015).

[81] S. Schröder, K. Ludwig, A. Aschikhin, R. D'Arcy, M. Dinter, P. González Caminal, S. Karstensen, A. Knetsch, V. Libov, and C. A. Lindstrøm *et al.*, Tunable and precise two-bunch generation at FLASHForward, Journal of Physics: Conference Series **1596**, 7 (2020).

[82] R. D'Arcy, V. Libov, and J. Osterhoff, A Transverse Deflecting Structure for the Plasma Wakefield Accelerator Experiment, FLASHForward, in *Proceedings of the International Beam Instrumentation Conference - IBIC2016* (Barcelona, 2016) pp. 759–762.

[83] D. Lipka, Cavity BPM Designs, Related Electronics and Measured Performances, in *Proceedings of the 9th European Workshop on Beam Diagnostics and Instrumentation for Particle Accelerators - DIPAC2009* (JACoW Publishing, Basel, Switzer-

land, 2009) pp. 280–284.

[84] C. Wiebers, M. Holz, G. Kube, G. Priebe, and H.-C. Schröder, Scintillating Screen Monitors for Transverse Electron Beam Profile Diagnostics At the European Xfel, in *Proceedings of the 2nd International Beam Instrumentation Conference - IBIC2013* (JACoW Publishing, Oxford, UK, 2013) pp. 807–810.

[85] M. Reukauff, *A low-noise front-end for an X-band particle detector at DESY*, Ph.D. thesis, Technische Universität Hamburg (2022).

[86] L. Fröhlich, A. Aghababyan, S. Grunewald, O. Hensler, U. F. Jastrow, R. Kammering, H. Keller, V. Kocharyan, M. Mommertz, and F. Peters *et al.*, The Evolution of the DOOCS C++ Code Base, in *Proceedings of ICALEPCS2021* (JACoW Publishing, 2021) pp. 188–192.

[87] V. Romano del Pozo, H. Bursali, N. Catalan Lasheras, A. Grudiev, S. L. Pitman, I. Syratchev, and M. Volpi, High Power Conditioning of X-band Variable Power Splitter and Phase Shifter, in *Proceedings of the 10th International Particle Conference - IPAC2019* (JACoW Publishing, Melbourne, Australia, 2019) pp. 2964–2967.

[88] P. Craievich, Z. Geng, F. Marcellini, C. Kittel, S. Reiche, T. Schietinger, G. Wang, and E. Prat, Post-undulator beam measurements with PolariX TDS in SwissFEL, in *Proceedings of the SPIE 2023* (2023).

[89] S. Schulz, I. Grguraš, C. Behrens, H. Bromberger, J. T. Costello, M. K. Czwalinna, M. Felber, M. C. Hoffmann, M. Ilchen, and H. Y. Liu *et al.*, Femtosecond all-optical synchronization of an X-ray free-electron laser, Nature Communications **6** (2015).

[90] S. Wesch, *Echtzeitbestimmung longitudinaler Elektronenstrahlparameter mittels absoluter Intensitäts- und Spektralmessung einzelner kohärenter THz Strahlungspulse*, Ph.D. thesis, Universität Hamburg (2012).

[91] J. W. Zhirong Huang, Microbunching Instability due to Bunch Compression, in *ICFA Beam Dynamics Newsletter*, 38 (2005) pp. 37–50.